Thesis Title

by

E. Ross

A thesis submitted to the

University of Birmingham

for the degree of

DOCTOR OF PHILOSOPHY

Solar and Stellar Physics Group (SASP)

School of Physics and Astronomy

University of Birmingham

Birmingham, B15 2TT

Month 20XX

Contents

List of Figures

List of Tables

List of Abbreviations

AR Active Region.

BIC Bayesian Informatin Criterion.

BiSON Birmingham Solar Oscillations Network.

EEMD Empirical Mode Decomposition.

GMF General Magnetic Field.

HiSPARC High School Project on Astrophysics and Research with Cosmics.

LOS Line Of Sight.

MCMC Markov Chain Monte Carlo.

MFC Magnetic Flux Concentration.

MMF Mean Magnetic Field.

PSD Power Spectral Density.

RM Rotationally Modulated.

RMS Root Mean Square.

RSS Resonant Scattering Spectrometer.

SB Stochastic Background.

SDO/AIA Solar Dynamics Observatory Atmospheric Imaging Assembly.

SDO/HMI Solar Dynamics Observatory Helioseismic and Magnetic Imager.

SMMF Solar Mean Magnetic Field.

WSO Wilcox Solar Observatory.

1 Galactic Cosmic Ray Behaviour During Solar Cycle 24

The majority of the text in this chapter is taken from Ross & Chaplin (2019). I was first author on this journal article and conducted the work of the investigation. Section 1.6 has been written since the publication of Ross & Chaplin (2019) to provide a comparative analysis using the High School Project on Astrophysics and Research with Cosmics (HiSPARC) data.

1.1 Introduction

Galactic cosmic rays (GCRs) are charged particles and atomic nuclei with energies spanning the range from a few MeV up to approximately 10^{21} eV, that encroach upon the Earth from all directions (Giacalone, 2010). They mainly originate outside the solar system, within the Milky Way; however they are also expected to originate from other galaxies (Aab et al., 2017). GCRs at the top of the atmosphere are mostly composed of protons ($\sim 87\%$) and α-particles ($\sim 12\%$), with a smaller contribution ($\sim 1\%$) from heavier nuclei (Dunai, 2010).

When cosmic rays (CRs) enter the atmosphere, they interact with atmospheric atoms and produce cascades of secondary particles, which at ground level are primarily neutrons and muons. Neutron monitors (NMs) and muon detectors (MDs) located at different locations on Earth have been used since the 1950s to observe GCRs. Information on GCRs prior to the modern epoch of NMs and MDs, and the

space age, rely on the studies of cosmogenic isotope records from ice cores and tree rings (Owens & Forsyth, 2013).

It has long been established that there exists an anti-correlation between GCR intensity and the level of solar activity, over a cyclic 11-year period, with perhaps some time-lag (Forbush, 1958; Parker, 1965; Usoskin et al., 1998; Van Allen, 2000). Figure 1.1 shows clearly the anti-correlation between GCRs and sunspot number (SSN).

It is well known that the 11-year solar activity cycle is in fact a 22-year cycle - the Hale cycle - which describes the alternating polarity of the large-scale solar magnetic field (Thomas et al., 2014a). The interchanging peaked and flat-topped shape of GCR intensity in Figure 1.1 is a manifestation of this effect in addition to other CR transport processes (Aslam & Badruddin, 2012).

The polarity of the solar field, A, is taken to be negative when the field axis is aligned with the axis of rotation, and positive when the opposite is true (Thomas et al., 2014a). The solar field polarity conventionally is described in combination with particle charge, q, due to the effect of curvature and gradient drift on charged particles; thus it is customary to define the solar polarity as qA. Vertical lines showing the approximate epochs at which the polarity reverses are plotted in Figure 1.1 (Janardhan et al., 2018; Thomas et al., 2014a).

Particle drifts differ during different qA cycles, with positive CRs (i.e. protons) predominantly arriving into the heliosphere from the heliospheric poles and outwards to Earth during periods when $qA > 0$, whereas when $qA < 0$, positive CRs predominantly arrive at Earth inwards along the heliospheric current sheet (HCS) (Belov, 2000; Thomas et al., 2014b). As the solar magnetic dipole axis is tilted to the solar rotation axis, so is the HCS; the HCS tilt varies with solar cycle and is typically smaller during solar minimum and larger during solar maximum (Owens & Forsyth, 2013). The tilt angle of the HCS has also been shown to be strongly correlated to the GCR intensity and the GCR lag behind the solar activity (Belov,
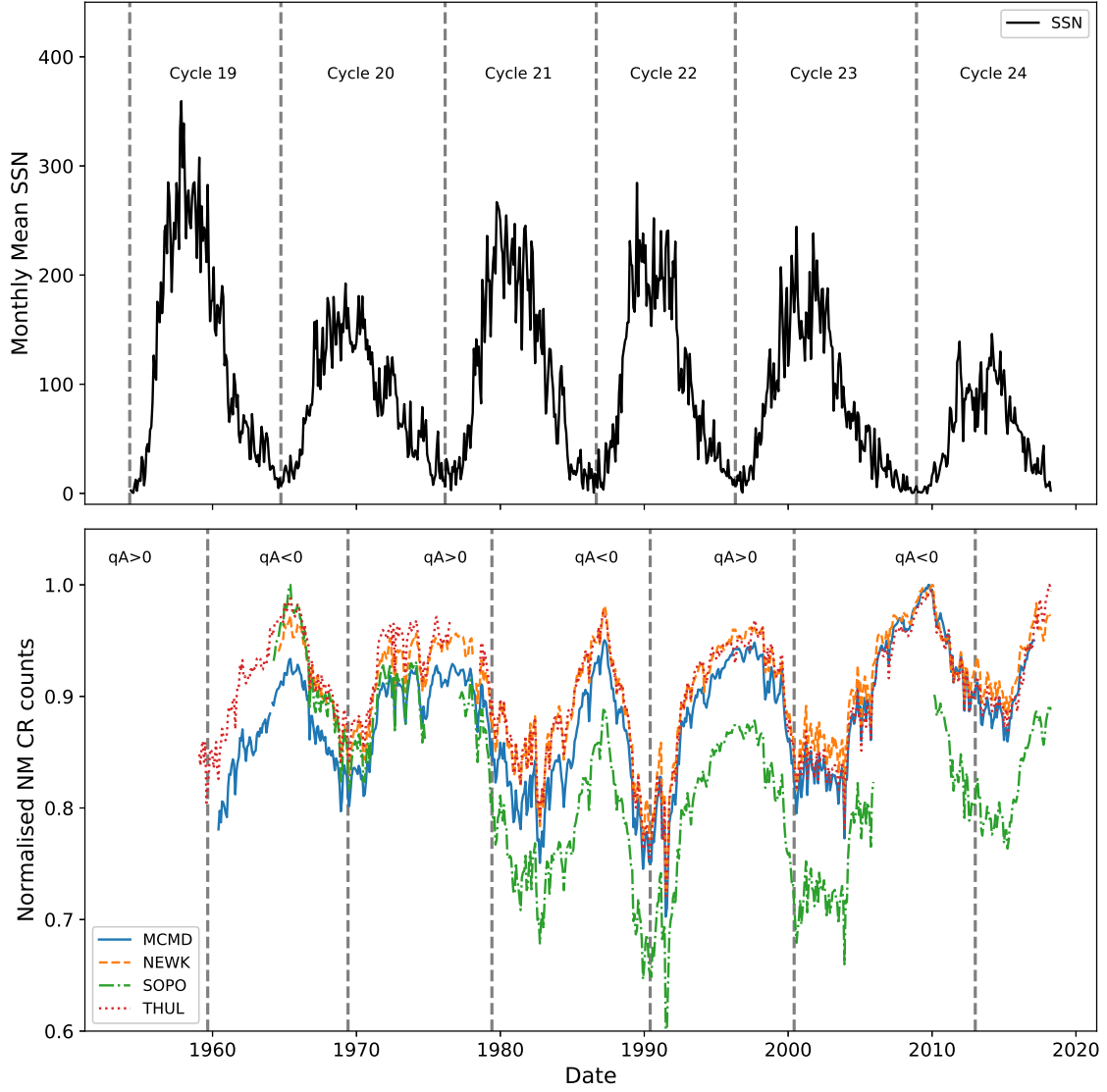
Figure 1.1: SSN (top), with vertical lines showing the beginning of each solar cycle. Cosmic ray intensity recorded by NMs (bottom), with vertical lines showing the approximate epochs of solar magnetic field polarity reversals. (MCMD = McMurdo, NEWK = Newark, SOPO = South Pole, THUL = Thule).

2000; Mavromichalaki et al., 2007).

Aslam & Badruddin (2012, 2015) found that the different processes of CR transport have varying levels of importance throughout the solar activity cycle, but around solar maximum it is likely that drifts play less of a role and disturbances in the solar wind (and hence HCS) are the predominant factor of CR modulation. Even cycles encounter $qA < 0$ polarity during their onset phase and $qA > 0$ during their declining phase, thus experiencing a faster GCR recovery after solar maximum as the GCRs predominantly enter the heliosphere from the heliospheric poles and experience an outwards drift towards Earth. Odd cycles encounter $qA > 0$ polarity during their onset phase and $qA < 0$ during their declining phase and so experience a slower recovery after solar maximum, as the GCRs predominantly enter the heliosphere along the HCS. When the HCS is tilted and disturbed during the declining activity phase, the path length that GCRs must travel to Earth increases; hence resulting in an increased time-lag.

Several studies have demonstrated the lag between GCR and solar activity proxies is approximately zero (i.e. no lag) during even solar cycles, and that there exists a lag of around a year or more during odd solar cycles (Usoskin et al., 1998; Mavromichalaki et al., 2007; Singh et al., 2008).

Van Allen (2000) showed through cross-plotting the annual mean intensity of GCRs against sunspot number (SSN) between 1953 and 1999 (covering solar cycles 19-22), that there is a distinct difference in the plot shapes between the different solar cycles, with 19 and 21 producing broad ovals, and 20 and 22 as approximately flat lines. The striking difference between odd-numbered and even-numbered cycles is shown for cycles 19-24 in Figure 1.2. It is believed that this hysteresis effect is caused by the combination of the heliospheric magnetic field (HMF), solar magnetic field polarity and thus the particle drift, and the tilt of the HCS leading to a slow recovery of GCR intensity after maxima in odd cycles and a fast recovery after maxima in even cycles (Van Allen, 2000; Belov, 2000; Thomas et al., 2014a).

4
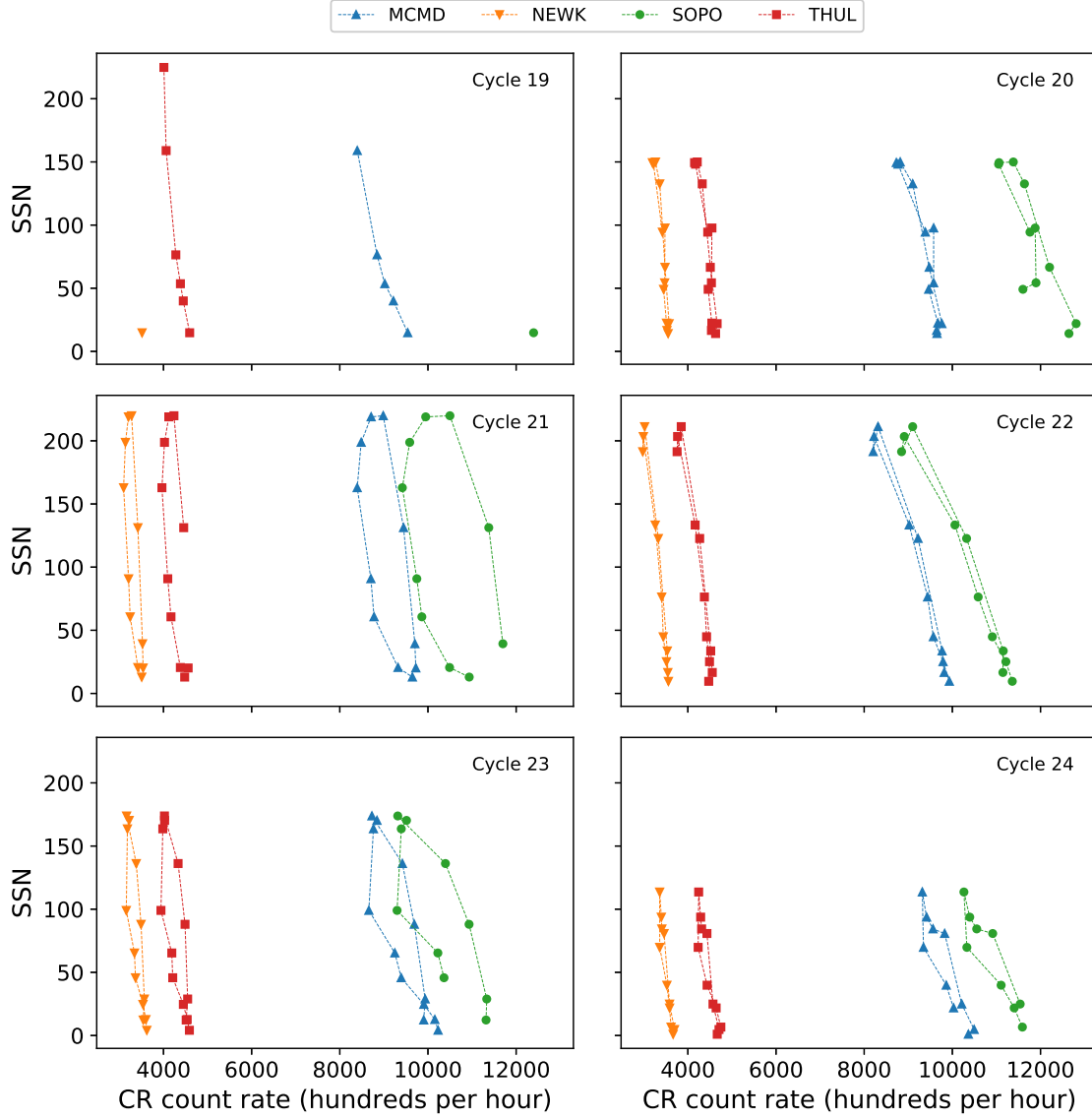
Figure 1.2: Hysteresis plots between yearly averaged SSN and yearly averaged GCR intensity for each of the 4 main NM stations over cycles 19-24.

An extension of this work has since been carried out by Inceoglu et al. (2014) showing that the even numbered solar activity cycles can be best modeled using a linear fit due to the narrow shape of the hysteresis loops; whereas odd-numbered solar activity cycles are better represented by ellipses due to their broader shape.

There has been speculation in the literature on the behaviour of cycle 24 compared to recent odd and even cycles. It has been suggested that there exists a lag between SSN maxima and GCR intensity minima in excess of 10 months (Kane, 2014; Mishra & Mishra, 2016) which does not follow the previous even cycles having a near-zero lag and in fact suggesting that cycle 24 behaved similarly to previous odd cycles; however these studies do not make use of a complete cycle of data and thus may draw inaccurate conclusions about the behaviour of the whole cycle because of the unusually extended nature of the declining phase of cycle 23 and the low amplitude of cycle 24 maximum (Broomhall, 2017). Mishra & Mishra (2016) make use of a more complete data set for cycle 24, yet still incomplete, and conclude that it is also likely that a 4 month lag could exist between GCRs and SSN.

This work aims to provide a timely update on the statistical relationship between GCR intensity and solar activity during solar cycle 24, since the cycle has now almost declined to a minimum. These aims have been achieved through a time-lag analysis and hysteresis effect analysis between SSN and GCR intensity.

In Section 1.2 we provide a brief description of the data that was used throughout this study for both CRs and SSN.

We show in Section 1.3 through a correlative time-lag analysis that there exists a small time-lag between the SSN and GCR intensity over solar cycle 24, which is slightly longer than preceding even-numbered cycles but not as high as observed in previous odd-numbered cycles. We also discuss whether the time-lag between SSN and GCR shows a dependence on the rigidity cut-off of the observing station.

In Section 1.4 we model the shapes of hysteresis plots between GCR intensity and SSN. We show that the behaviour of the hysteresis loops for cycle 24 follow the

preceding even-numbered solar activity cycles and is better represented by a straight line fit rather than an elliptical model.

1.2 Data

For the majority of the work in this study we have considered the pressure corrected count rates measured by four NM monitor stations as acquired from the NM data base (NMDB, 2018) event search tool (NEST) (http://nmdb.eu/nest/). The four stations are McMurdo (MCMD), Newark (NEWK), South Pole (SOPO), and Thule (THUL), i.e. the same NM stations used in the study by Inceoglu et al. (2014) to provide a comparison to existing literature. Table 1.1 details the basic characteristics of the NM stations used in this study.

We have investigated the long-term GCR modulation in the heliosphere from 1964-2018, spanning solar cycles 20-24, for the cycle epochs: 20: (10/1964 - 03/1976); 21: (03/1976 - 09/1986); 22: (09/1986 - 05/1996); 23: (05/1996 - 12/2008); 24: (12/2008 - 03/2018). Early predictions on solar cycle 25 suggest that solar cycle 24 is unlikely to reach a minimum earlier than the middle of 2019 up to as far as early 2021 (see Howe et al. (2018); Upton & Hathaway (2018); Pesnell & Schatten (2018)). The data used in this study are therefore of an incomplete cycle 24; however we believe this to now have a minimal effect on the results as cycle 24 draws to a minimum. Cycle 19 was omitted from this study due to the incomplete data set for this period (see Figure 1.1 and Figure 1.2).

During the time-lag correlation analysis, as our results suggested there may be a rigidity dependence on the time lag, we introduced a further 12 NM stations with data acquired from NEST spanning cycles 20-24 to increase the rigidity spectrum utilised in this study; these stations and their basic characteristics are also detailed in Table 1.1. These stations are not included in the rest of the results however as the results from these stations do not change the conclusions of this study.

Furthermore, we have also used monthly/yearly averaged SSN, as collected by

Table 1.1: Neutron monitor stations used in this study and their vertical geomagnetic cut-off rigidity (R_c), longitude, latitude, and altitude acquired from NEST. The first four stations have been used for all of the analysis while the lower 12 stations have been used exclusively for the investigation into the dependence of R_c on the time-lag.

		Station	R_c [GV]	Long. [deg]	Lat. [deg]	h [m]
Time-Lag &	Hysteresis	McMurdo (MCMD)	0.30	166.6 E	77.9 S	48
		Newark (NEWK)	2.40	75.8 W	39.7 N	50
		South Pole (SOPO)	0.10	0.0 E	90.0 S	2820
		Thule (THUL)	0.30	68.7 W	76.5 N	26
R$_c$ dependence	of time-lag	Oulu (OULU)	0.81	25.5 E	65.1 N	15
		Kerguelen (KERG)	1.14	70.3 E	49.4 S	33
		Magadan (MGDN)	2.10	151.1 E	60.0 N	220
		Climax (CLMX)	3.00	106.2 W	39.4 N	3400
		Dourbes (DRBS)	3.18	4.6 E	50.1 N	225
		IGY Jungfraujoch (JUNG)	4.49	7.98 E	46.6 N	3570
		Hermanus (HRMS)	4.58	19.2 E	34.4 S	26
		Alma-Ata B (AATB)	6.69	76.9 E	43.0 N	3340
		Potchefstroom (PTFM)	6.98	27.1 E	26.7 S	1351
		Mexico (MXCO)	8.28	99.2 W	19.8 N	2274
		Tsumeb (TSMB)	9.15	17.6 E	19.2 S	1240
		Huancayo (HUAN)	12.92	75.3 W	12.0 S	3400

WDC-SILSO (http://sidc.be/silso/), for the time-lag analysis/hysteresis analysis respectively as our chosen proxy of solar activity.

1.3 Time-Lag Analysis

1.3.1 Method

To investigate the time delay between the modulation of GCRs compared to the solar activity, a time-lag cross-correlation analysis was performed between monthly mean GCR intensity and monthly mean SSN for each station, following the approach of Usoskin et al. (1998). We used a time window of width T centred on a time t, i.e. shifting within the interval $t - T/2$ to $t + T/2$. Here we used $T = 50$ months.

The window was shifted in steps $\Delta t = 1$ month within this interval and for each step the Spearman's rank correlation coefficient (ρ) between GCR intensity and SSN was calculated. The lag between GCR and SSN was then estimated by finding the peak correlation coefficient within the time interval T.

The results from the four main NM stations used suggested that there may be a relationship between the rigidity cut-off (R_c) of a NM station and the time-lag for GCRs; hence four additional NM stations were introduced to determine whether this was so, as detailed above.

1.3.2 Results

The correlation (ρ) between monthly averaged GCR counts and SSN for different time-lags was calculated for cycles 20-23. The variation in ρ is presented in Figure 1.3, showing that for each cycle there is a time-lag corresponding to peak anti-correlation between GCR intensity and SSN. Table 1.2 summarises the time-lag with the highest correlation and the corresponding correlation coefficient for all stations in each individual solar cycle.

As previously reported in the literature, we see here that all of the NM stations clearly exhibit almost no lag during even solar cycles, and a longer lag varying
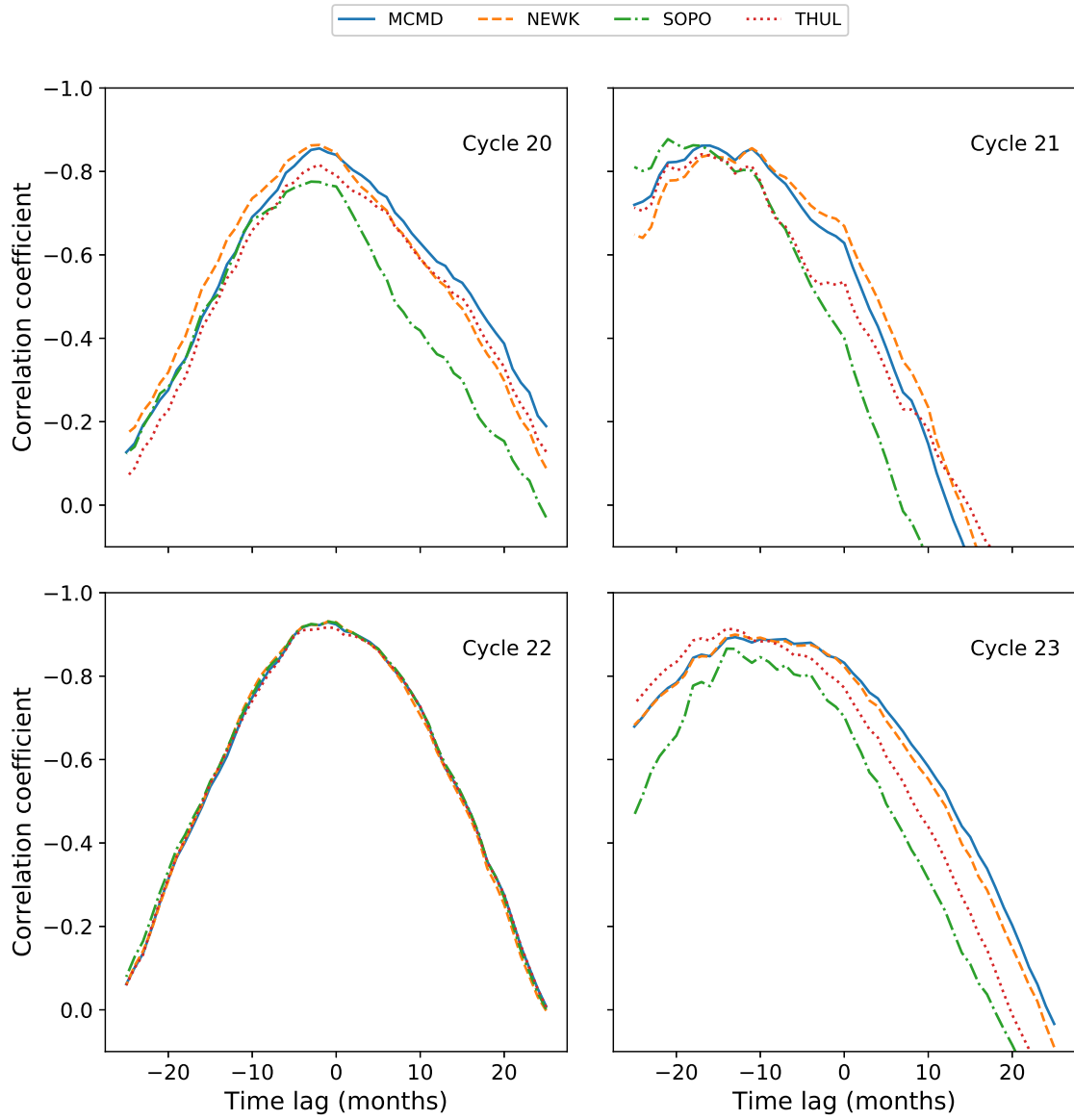
Figure 1.3: Variation in the correlation coefficient with time-lag NM station GCR intensity and SSN during solar cycles 20-23.

Table 1.2: Time-lags and the corresponding cross-correlation coefficient between NM CR count and SSN for solar cycles 20-23.

| | Cycle 20 | | Cycle 21 | |
	Lag [months]	ρ	Lag [months]	ρ
McMurdo	2	-0.855	16	-0.862
Newark	2	-0.863	11	-0.856
South Pole	3	-0.776	21	-0.877
Thule	2	-0.816	17	-0.841
	Cycle 22		Cycle 23	
	Lag [months]	ρ	Lag [months]	ρ
McMurdo	1	-0.929	13	-0.894
Newark	1	-0.931	13	-0.900
South Pole	1	-0.931	14	-0.866
Thule	1	-0.917	14	-0.914

between 11-21 months during odd solar cycles. There is a strong agreement between the results presented in Table 1.2 and those of Mavromichalaki et al. (2007), Kane (2014), and Paouris et al. (2015), thus providing further evidence on the distinction between odd and even solar cycles due to particle transport in the heliosphere. The agreement with existing literature provides evidence of a suitable methodology in this study.

The same cross-correlation technique was then applied to cycle 24 between the dates 12/2008 - 03/2018 and the results are presented in Figure 1.4 and Table 1.3.
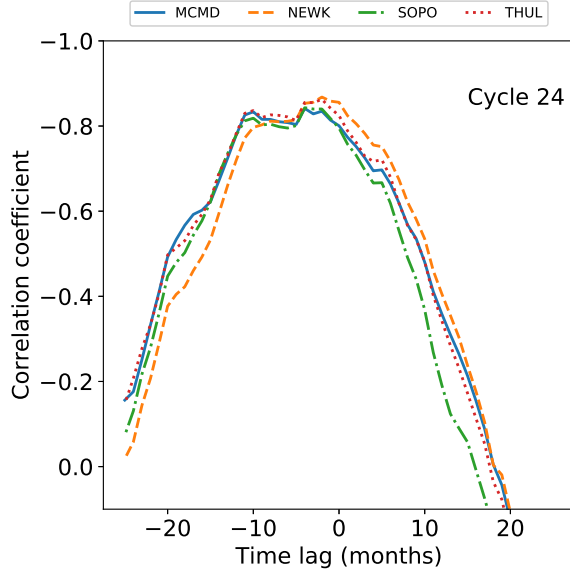
Figure 1.4: Variation in the correlation coefficient with time-lag between NM GCR intensity and SSN during solar cycle 24.

Table 1.3: Time-lags and the corresponding cross-correlation coefficient between NM GCR intensity and SSN for solar cycle 24.

	Cycle 24	
	Lag	ρ
	[months]	
MCMD	4	-0.841
NEWK	2	-0.868
SOPO	4	-0.843
THUL	2	-0.862

Cycle 24 is seen here to follow the pattern of almost no lag for even cycles; however cycle 24 does display a lag that is larger than the previous two even-numbered cycles, despite not being as large as the two previous odd-numbered cycles. The cause for the increased time-lag in cycle 24, as compared to the previous two even-numbered cycles, is likely due to the combined effects of the unusually deep and extended minimum between solar cycles 23 and 24, which delayed the decline in GCR intensity and caused record-breaking high GCR intensities (Pacini & Usoskin, 2015), and the small amplitude of the cycle 24 maximum.

The results presented in this study, using data for a near-complete cycle 24, show that the results of Kane (2014), and Mishra & Mishra (2016), were likely unduly influenced by the unusually deep and extended declining phase of cycle 23 given that they had a limited data set. Mishra & Mishra (2016) used data for just over half of cycle 24 and resulted in a time-lag of 4 months which agree with the results of this study.

As a further note on time-lag, Tomassetti et al. (2017) showed that through the introduction of time-lag as a parameter in the CR transport calculations of CR spectra that there exists a time-lag of 8.1 ± 1.2 months during the period 2000-2012

spanning across cycle 23 and 24. We performed the time-lag analysis for the first 4 NM stations detailed in Table 1.1 for the period between 2000-2012 to investigate whether these results can be reproduced. The results of this analysis are presented in Figure 1.5 and Table 1.4.
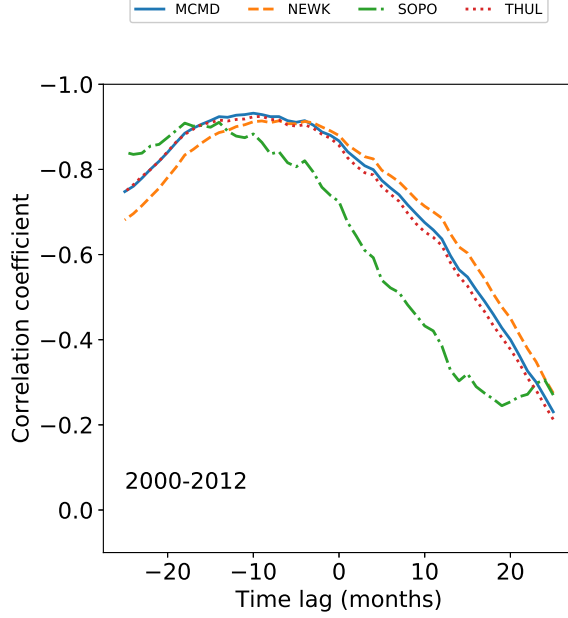
Table 1.4: Time-lags and the corresponding cross-correlation coefficient between NM GCR intensity and SSN during 2000-2012.

	2000-2012	
	Lag [months]	ρ
MCMD	10	-0.932
NEWK	7	-0.914
SOPO	14	-0.911
THUL	9	-0.925

Figure 1.5: Variation in the correlation coefficient with time-lag between NM GCR intensity and SSN between 2000-2012.

From the time-lag analysis of the 4 stations presented there is a mean lag of 10.00 ± 1.47 months, which is in good agreement with the results of Tomassetti et al. (2017).

Finally, allowing for the odd/even cycle dependence, we see in Figure 1.3, Figure 1.4, and Figure 1.5 that the time-lag appears to depend on the rigidity of the NM station used for observation. Such a dependence may impact the conclusions depending on the choice of NM station. We expect that if a dependence exists, a station with a higher rigidity cut-off (R_c) would have a shorter lag as this station observes higher energy CRs which are affected less by solar modulation and thus able to recover faster from solar maximum. Whereas a station with a lower cut-off rigidity observing lower energy CRs, which are more influenced by solar modulation, would recover more slowly from solar modulation and therefore experience a
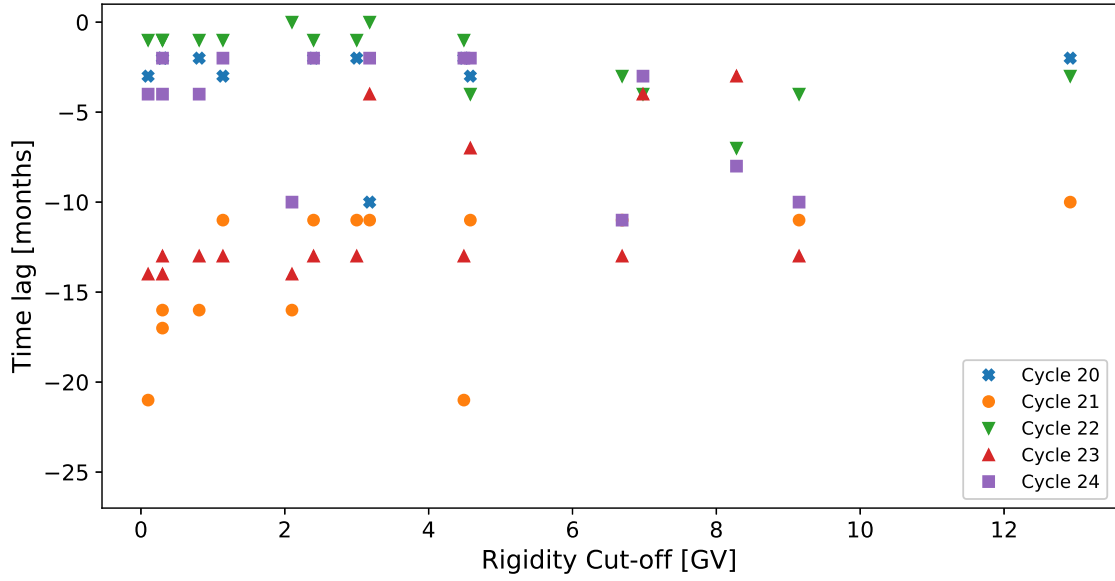
Figure 1.6: Variation in time-lag plotted against NM station rigidity cut-off for the 16 NM stations detailed in Table 1.1.

longer time-lag. This is supported by Figure 1.3, Figure 1.4, and Figure 1.5, but in order to provide more conclusive evidence of such a relationship we introduced the additional NM stations detailed in Table 1.1 to provide a rigidity range spanning 0-13 GV. We present in Figure 1.6 a plot of the time-lag versus station R_c for all 16 stations over cycles 20-24. To acquire uncertainties on the time-lag we ran 1000 Monte Carlo simulations of the time-lag analysis, sampling from the uncertainty distributions for each of the monthly averaged SSN and GCR counts; however the uncertainties in the data propagated in the Monte Carlo simulations produced no scatter in the overall results.

The results of this analysis do not show a clear rigidity dependence on the time-lag between SSN and GCR intensity; the sampling of higher R_c is too low, due to the availability of high R_c stations, to reasonably conclude on such a dependence at high rigidities, despite cycle 21 suggesting the existence of a dependence for low R_c stations as per our expectations. For low R_c stations there appears to be a more pronounced distinction between the time-lag observed between odd-numbered and even-numbered cycles than for higher R_c stations, however again this is not definitive

due to the low sampling at higher R_c. We therefore conclude that there will be no significant dependence of the time-lag analysis on the R_c of the observing station.

1.4 Hysteresis Effect Analysis

1.4.1 Method

To investigate the hysteresis effect, we have adopted the approaches of Van Allen (2000), Singh et al. (2008), and Inceoglu et al. (2014). Plots of the annual mean SSN versus the annual mean GCR intensity were generated for cycle 20-24 and analysed by fitting different models to the data.

As highlighted in Inceoglu et al. (2014), even-numbered solar cycles can be suitably modeled by a linear fit due to their narrow hysteresis shape, and odd-numbered solar cycles were shown to be better modeled by ellipses due to their broadened hysteresis shape. Here, we first repeated for solar cycles 20-23 the linear and ellipse fitting to confirm the method reproduces the results reported in Inceoglu et al. (2014) before applying the method to cycle 24.

For even cycles which display narrow hysteresis loops, an unweighted least squares linear regression was used to reconstruct estimates of the GCR intensity from SSN. As odd-numbered solar cycles display a broader hysteresis loop, they were separately modeled using unweighted linear regression and ellipse fitting to determine the model providing the better fit.

The equation of the ellipse fitting took the form:

$$
\begin{bmatrix} x \\ y \end{bmatrix} = \begin{bmatrix} x_0 \\ y_0 \end{bmatrix} + R(\phi) \begin{bmatrix} a \, \cos\theta \\ b \, \sin\theta \end{bmatrix}
\tag{1.1}
$$

where x is GCR intensity; y is SSN; (x_0, y_0) are the centroid coordinates of the fitted ellipse, $R(\phi)$ is the rotation matrix; ϕ is the ellipse tilt angle; a and b are the semi-major and semi-minor axes respectively; and $0 \leq \theta \leq 2\pi$ is the polar angle measured anti-clockwise from the semi-major axis.

In order to regain the GCR intensity from the model, where linear regression was used to model the data, GCR was acquired directly from the SSN for each year. For the ellipse model the GCR was acquired from the model as a function of time from θ, where the time-lag calculated from the analysis in Section 1.3 was used to correctly phase the ellipse allowing θ to be calculated using standard equations of ellipses.

GCR intensity predicted by the linear regression and ellipse models were compared to the measured GCR intensity using Spearman's rank correlation as per Inceoglu et al. (2014).

1.4.2 Results

The hysteresis loops between yearly averaged SSN and GCR intensity for each station were first modeled with a linear regression for both odd and even solar activity cycles, then the odd cycles were separately re-modeled by ellipse fitting to show that this provides a more representative fit as suggested in Inceoglu et al. (2014). The correlation between measured CR intensities and modeled CR intensities for cycles 20-23 are presented in Table 1.5.

Table 1.5: Correlation coefficients of the linear regression and ellipse modeling of the hysteresis plots for solar cycles 20-23.

| | Cycle 20 | | Cycle 21 | | Cycle 22 | | Cycle 23 | |
	Linear	Ellipse	Linear	Ellipse	Linear	Ellipse	Linear	Ellipse
McMurdo	0.867	-	0.664	0.946	0.964	-	0.846	0.852
Newark	0.888	-	0.700	0.964	0.955	-	0.857	0.874
South Pole	0.746	-	0.358	0.939	0.936	-	0.733	0.855
Thule	0.783	-	0.912	0.964	0.900	-	0.813	0.929

There is a consistent and good agreement between the measured and modeled CR intensities for even solar cycles modeled through linear regression, because the hysteresis loops are quite narrow as shown in Figure 1.7. These results support the findings of Inceoglu et al. (2014). Note that discrepancies in the correlation coefficients between this study and Inceoglu et al. (2014) are likely due to a number

16
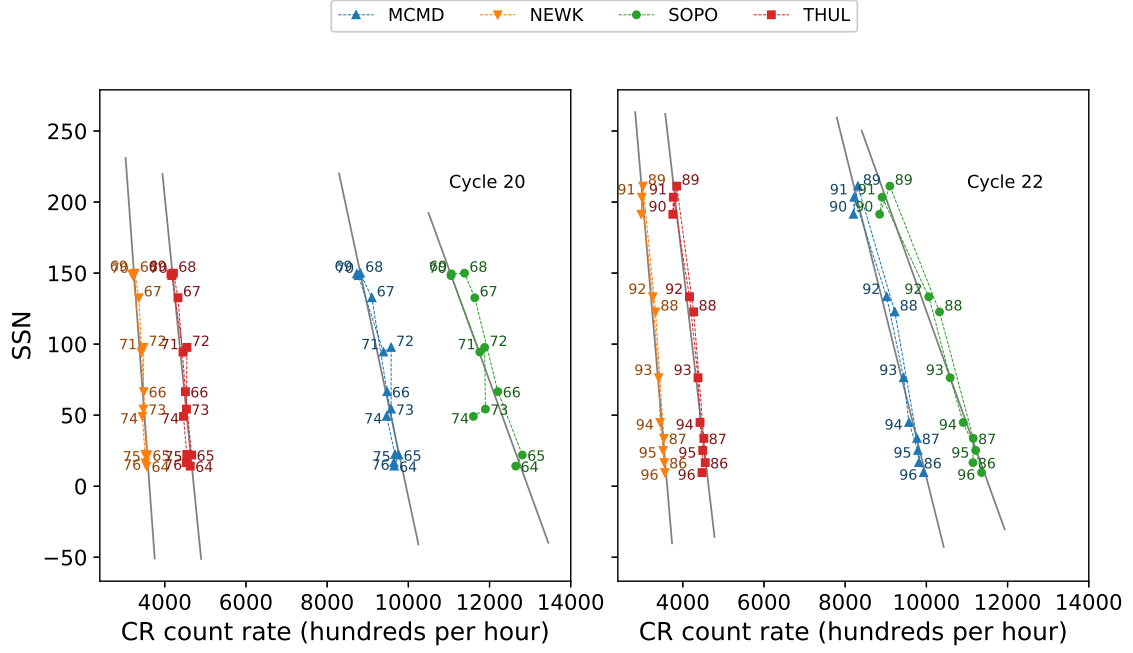
Figure 1.7: The hysteresis plots for even solar cycles 20 and 22 and the linear regression fit to the data.

of reasons: Inceoglu et al. (2014) used data smoothing processes where in this study raw data are used; Inceoglu et al. (2014) made use of monthly mean data, whereas annual mean data was used in this study; Inceoglu et al. (2014) interpolated missing data, whereas gaps have been left untreated in this study.

The linear relations for odd solar cycles are less consistent in their agreement with observed CR intensities, with the correlation during cycle 21 as low as 0.34 for South Pole and as high as 0.91 for Thule. Across both of the odd cycles considered in this study linear regression is not as good a representation of the data as for even cycles. Figure 1.8 shows the wider hysteresis loops which is a characteristic of odd solar cycles and shows visually that a linear fit does not provide a good representation of the data.

In agreement with the results of Inceoglu et al. (2014), it can be seen from the results in Table 1.5 that the ellipse models provide estimates of the CR intensity which are in good agreement with the measured intensities due to the increased correlation coefficient for each station during cycle 21 and cycle 23; for SOPO during
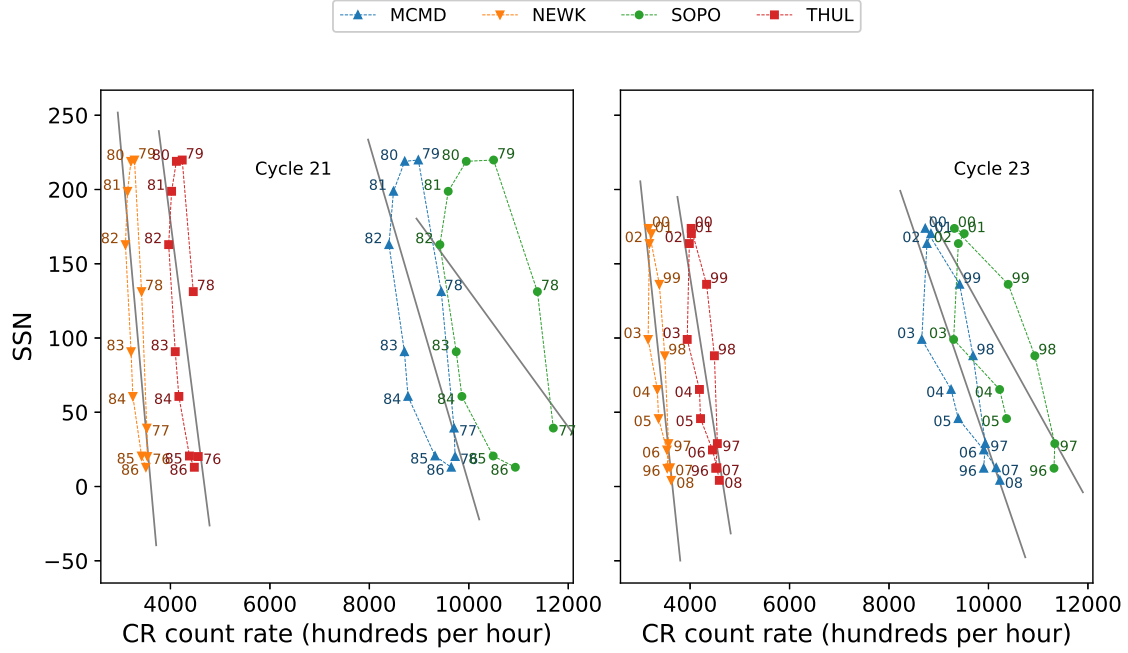
Figure 1.8: The hysteresis plots for odd solar cycles 21 and 23 and the linear regression fit to the data.

cycle 21 the increase in ρ is seen to be 0.58 proving the benefit of the ellipse model.

If cycle 24 follows the pattern between odd and even cycles, it is expected that the best fit will be provided by the linear model; however it can be seen in Figure 1.2 that cycle 24 appears to display a wider hysteresis loop than the two preceding even-numbered cycles. Both the linear model and ellipse model were applied to the hysteresis plots for solar cycle 24 to determine which model would provide the better fit; the correlation between measured CR intensities and modeled CR intensities are presented in table 1.6.

Table 1.6: Correlation coefficients of the linear regression and ellipse modeling of the hysteresis plots for solar cycle 24.

| | Cycle 24 | |
	Linear	Ellipse
McMurdo	0.903	0.927
Newark	0.936	-
South Pole	0.883	-
Thule	0.873	0.936

The linear model for cycle 24 shows a good correlation between the observed
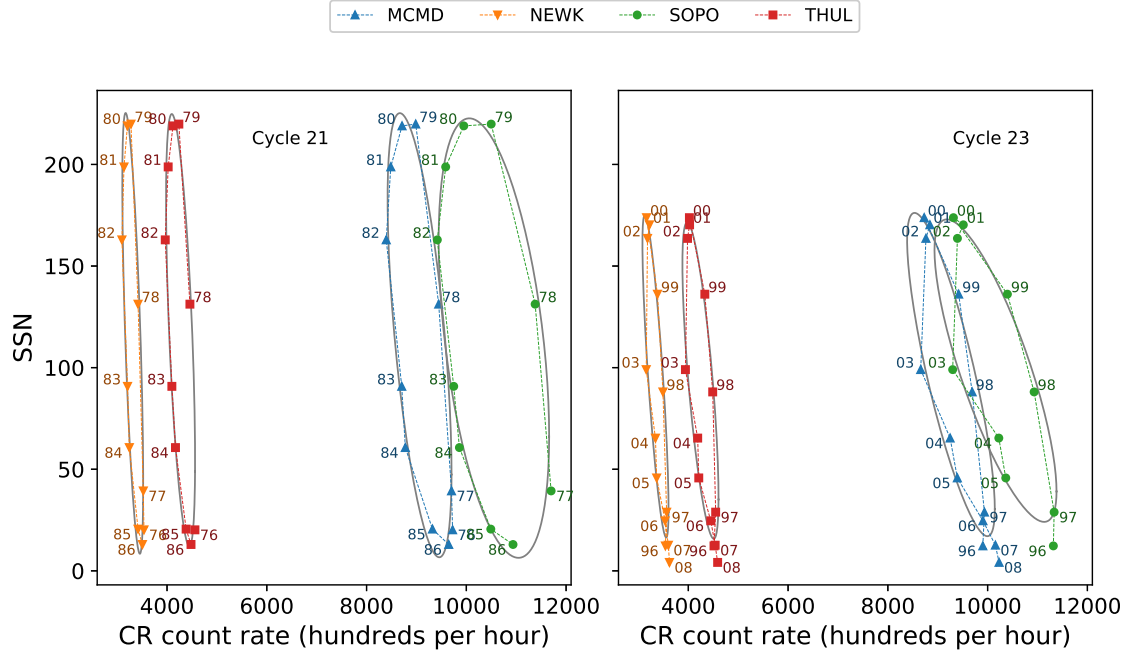
Figure 1.9: The hysteresis plots for odd solar cycles 21 and 23 and the ellipse fit to the data.

and modeled CR intensities providing evidence to suggest that cycle 24 follows the two preceding even-numbered cycles. The ellipse model does however improve the relation between the observed and modeled CR intensities for 2 out of the 4 stations: McMurdo and Thule. For South Pole and Newark the ellipse model was not able to provide a fit at all, which is believed to be due to the Newark data points crossing where the semi-major axis would be defined for the ellipse model causing the calculation of the semi-major and semi-minor axes to return as not a number, and the South Pole has data missing at the beginning of cycle 24.

The results for solar cycle 24 do not provide a conclusive answer as to whether cycle 24 behaves like past even solar cycles or odd cycles from this data set alone; however the ellipse model does not provide as significant an improvement for the two modeled NM stations as for odd cycles. The small improvement in the ellipse fit is likely due again to the effects of the extended declining phase of cycle 23 and the unusually low activity of cycle 24.

We repeated the analysis for the additional 4 NM stations that featured in this
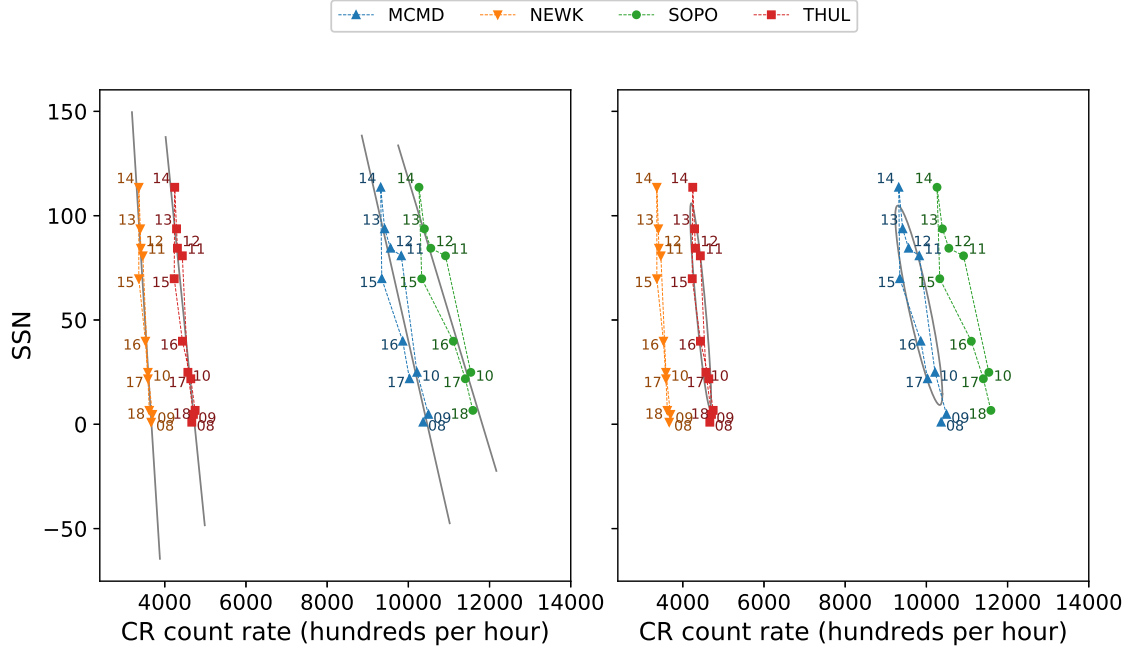
Figure 1.10: The hysteresis plot for solar cycle 24, and the linear regression fit to the data (left) and ellipse fit to the data (right).

study. Again, the linear model provided a good fit to the data however the ellipse model was not able to provide a fit; favouring the conclusion that cycle 24 is best represented by a simple linear model as was true for the preceding even-numbered cycles.

Despite cycle 24 having not yet declined to a minimum, it is clear from the observations shown in the hysteresis plots that further data in cycle 24 is unlikely to broaden the loop any further. The hysteresis loop begins to tighten up after 2016 following the broadening between 2014-2016; hence it appears unlikely that by the end of cycle 24 further observations will support the ellipse model and instead will favour the linear fit to the data.

1.5 Conclusions

As cosmic rays are modulated by the heliosphere during the 11-year solar activity cycle, and this effect has been studied for previous solar cycles, the principal aim of this study was to investigate the nature of GCRs during the current activity cycle

24 as it draws to a minimum.

In this study we presented a time-lag analysis between GCR intensity and SSN which showed that cycle 24 has a longer lag (2-4 months) than the preceding even-numbered solar activity cycles (typically 0-1 months); however its lag is not as large as preceding odd-numbered cycles, and cycle 24 follows the trend of a short or near-zero lag for even-numbered cycles. We suggest here that the cause of the extended lag in cycle 24 compared to previous even-numbered cycles is likely due to the deep, extended minimum between cycle 23 and 24, and the low maximum activity of cycle 24 (Broomhall, 2017).

It has been previously shown in the literature that there is a striking difference in the shape of the plot of SSN and GCR intensity between odd-numbered and even-numbered solar cycles. Due to the difference in the shape of the hysteresis plots for odd-numbered and even-numbered cycles, we have modeled the hysteresis plots using both a simple linear model and an ellipse model. The results of this study tend to support that cycle 24 follows the same trend as preceding even-numbered cycles and is best represented by a straight line rather than an ellipse, such is the case for odd-numbered activity cycles.

We emphasise that although cycle 24 has not yet ended, the shape of the hysteresis plots suggest that we are now past the main broadening region and the inclusion of further data for cycle 24 will very likely only support the linear model. This study will continue to follow the evolution of the cycle 24 until the onset of cycle 25, in around 2019-2021 (Howe et al., 2018; Upton & Hathaway, 2018; Pesnell & Schatten, 2018), when an update on the final results of cycle 24 should be provided.

1.6   Comparison with HiSPARC

The analysis was repeated using data from HiSPARC station 501, over the period between 2008 − 2019, to investigate whether the HiSPARC (HS) network was capable of monitoring the solar cycle variation in the muon count rate. HiSPARC station

501 was the best candidate for this analysis due to its long operational lifetime, in comparison to other HS stations, which spans most of cycle 24, and due to the fact that this station is used as the *gold standard* HS station.

This was further motivated by the observations of Fan & Velthuis (2018), in which they stated a confirmation of the accepted anti-correlation between solar activity and CRs after analysing the count rate of the HS 501 station, up to 2016/17, comparing the count rate with the number of solar flares and the SSN during the rising phase of cycle 24. We also wanted to determine whether the results of the analysis for the behaviour of GCRs during cycle 24, using HS data, agreed with those acquired above, using NM data.

A plot of the HS 501 data over this period is given in Figure 1.11, which shows a comparison between the HS count rate and SSN. By-eye, no clear anti-correlation is displayed between the HS count rate and the SSN.
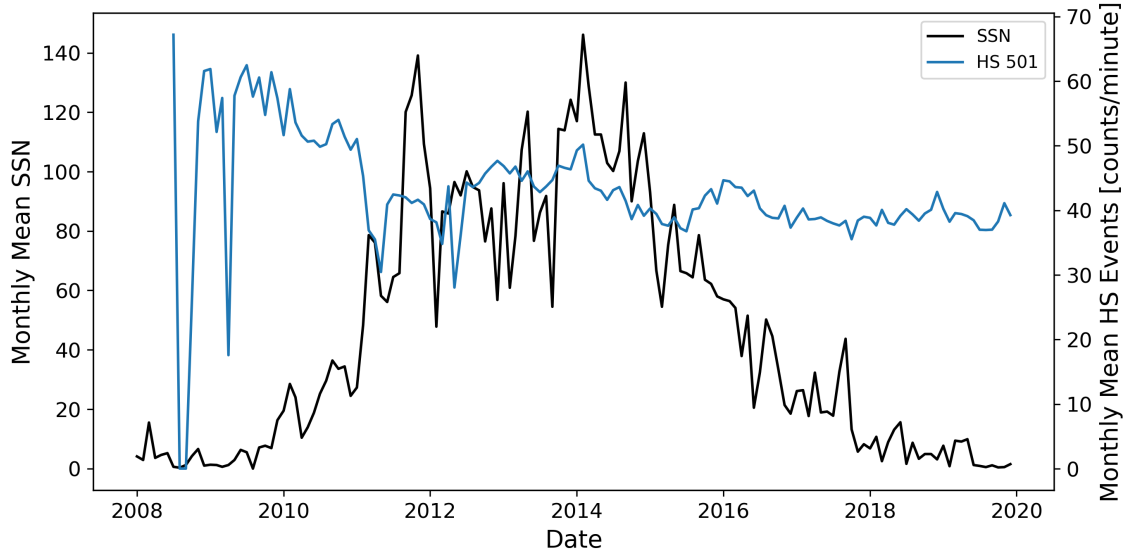
Figure 1.11: The monthly-mean CR-induced muon count rate recorded by HiSPARC (blue), and the SSN (black) between 2008 – 2019.

The spearman correlation coefficient between the HS count rate and the SSN was calculated between the two data sets, without performing the time-lag analysis, to be, $\rho = 0.078$. It was quantitatively concluded therefore that there exists no correlation between the SSN and the HS muon count rate, confirming what was

suspected by-eye.

This lack of anti-correlation is, unfortunately, symptomatic of the set-up of the HS stations. The set-up of the HS stations limits the capability of HS to observe the solar cycle modulation of CR intensity, because in many stations the detector voltages and threshold settings are regularly changed. The HiSPARC stations are typically set up to achieve a singles rate of around 100 Hz above the higher threshold limit, resulting in an events rate of around 1 Hz for the station (Fokkema, 2012). The PMT voltages are often adjusted when the count rate strays away from the nominal value, and this mitigates the ability of HiSPARC to reliably observe the solar cycle variation.

Modifications to the PMT voltage of each detector in HS 501 is illustrated in Figure 1.12, and shows the scale of the adjustments, with the voltages varying by as much as ~ 80 V. The effect of varying the PMT voltage is dependent on the individual PMT, but a change of 50–100 V will have an effect on the count rate, therefore it is likely to be a root cause for not observing the solar cycle modulation.
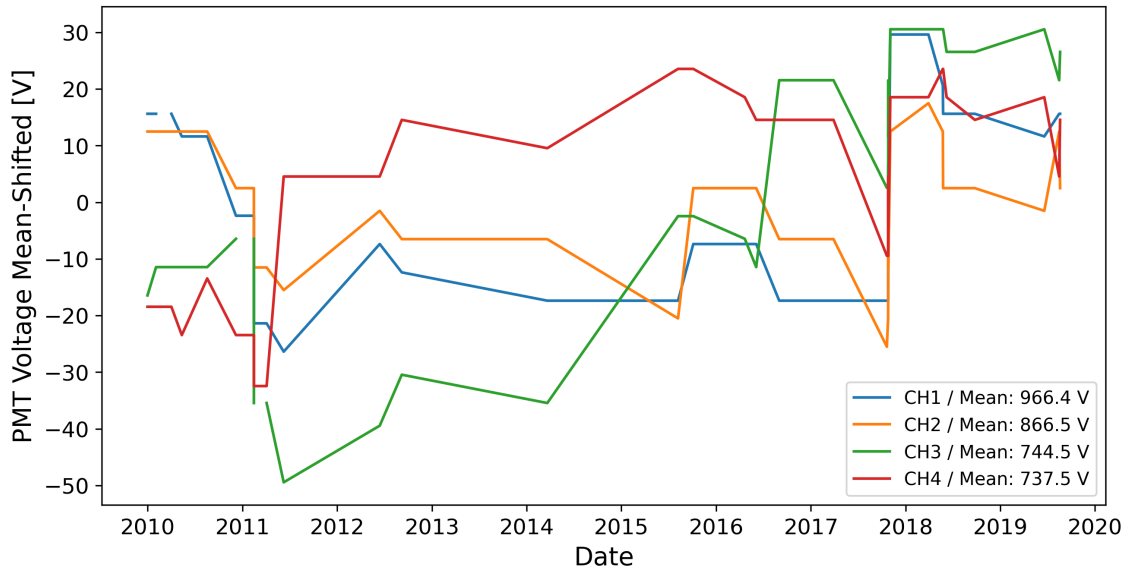
Figure 1.12: The evolution of the mean-shifted PMT operating voltages for each detector within HiSPARC station 501 between 2010 – 2020.

The claim that the solar cycle variation was observed in the count rate of HS 501

by Fan & Velthuis (2018) was highly likely based on their limited data set, spanning not enough of solar cycle 24. One could be convinced from the count rate during the rising phase of cycle 24 that the cycle variation is observed, but clearly beyond 2016 this relationship does not continue. It will be extremely interesting to re-visit this analysis of the HiSPARC data at the end of solar cycle 25, and particularly to repeat this analysis with the data from the new station configuration, HiSPARC station 14008.

2 A Frequency Domain Investigation on the Morphology of the Solar Mean Magnetic Field

2.1 Introduction

The Sun has a complicated magnetic field structure; many features of the Sun and proxies for the solar activity are related to the evolution of the Sun's magnetic field (Wu et al., 2018).

The Solar Mean Magnetic Field (SMMF) is a surprising, non-zero measurement of the imbalance of opposite magnetic flux polarities observed on the full, visible disc of the Sun (Svalgaard et al., 1975), and is defined as the mean Line Of Sight (LOS) magnetic field when observing the Sun-as-a-star (Scherrer et al., 1977a,b; Garca et al., 1999). In the literature the SMMF is also sometimes referred to as the General Magnetic Field (GMF) (Severny, 1971) or the Mean Magnetic Field (MMF) (Kotov, 2008) of the Sun.

Observations of the SMMF have typically been made by measuring the Zeeman splitting of spectral lines using a ground-based Babcock-type magnetograph (Scherrer et al., 1977a), although more recently the SMMF has been calculated from full-disc LOS magnetograms taken from space-borne telescopes such as the Solar Dynamics Observatory Helioseismic and Magnetic Imager (SDO/HMI), in order to

understand the morphology of the SMMF (Kutsenko et al., 2017; Bose & Nagaraju, 2018). It is understood that the strength of the SMMF may vary depending on the spectral line used to measure the SMMF (Kotov, 2008, 2012); however, the SMMF varies slowly with the solar activity cycle, with an amplitude on the order of a Gauss during solar maximum and a tenth of a Gauss during solar minimum (Plachinda et al., 2011). In addition, the SMMF displays a strong, quasi-coherent rotational signal, which must arise from inhomogeneities on the solar disc with lifetimes of several rotations (Chaplin et al., 2003; Xie et al., 2017).

Despite existing literature on SMMF observations spanning several decades, ultimately, the origin of the SMMF remains an open question in solar physics. The principle component of the SMMF is commonly assumed to be weak, large-scale magnetic flux, distributed over vast areas over the entire solar disc, rather than from more concentrated regions such as Active Regions (ARs) or sunspots (Severny, 1971; Scherrer et al., 1977a; Xiang & Qu, 2016). However, conversely, Scherrer et al. (1972) found that the SMMF was most highly correlated with flux from only the inner-most one quarter, by area, of the solar disc, which is more sensitive to active latitudes.

In recent literature, Bose & Nagaraju (2018) provided a novel approach to understanding the SMMF whereby they decomposed the SMMF through feature identification and pixel-by-pixel analysis of full-disc magnetograms. Bose & Nagaraju (2018) concluded that: (i) the observed variability in the SMMF lies in the polarity imbalance of large-scale magnetic field structures on the visible surface of the Sun, (ii) the correlation between the flux from sunspots and the SMMF is statistically insignificant, (iii) and more critically that the background flux dominates the SMMF, accounting for around 89% of the variation in the SMMF. However, there still remained a strong manifestation of the rotation in the background magnetic field presented by Bose & Nagaraju (2018). This is indicative of inhomogeneous magnetic features with lifetimes on the order of several solar rotations rather than

the shorter-lived, weaker fields usually associated with the large-scale background. It therefore raises the question of whether their technique assigned flux from Magnetic Flux Concentrations (MFCs) or ARs to the background.

In order to identify the contours of specific features Bose & Nagaraju (2018) used an adaptive thresholding technique on various Solar Dynamics Observatory Atmospheric Imaging Assembly (SDO/AIA) images of the solar disc to create binary masks for different types of features. These masks were then applied to scaled SDO/HMI magnetograms in order to separate the features on the disc and their contribution to the SMMF. Upon a closer inspection of the example magnetogram in Figure 2 of the paper, with over-plotted contours of identified features from SDO/AIA images, there are clearly regions of strong MFCs in the local vicinity of, and connected to, the identified features that lie outside their contour lines and are therefore allocated to the background magnetic field, rather than attributed to the specific features. It seems an obvious statement to suggest that SDO/AIA optical counterparts of the magnetograms will not exactly align with the observed magnetic flux in the magnetograms. We expect that the magnetic field will manifest itself differently in the optical observations and the magnetograms, which leads one to believe that the background component in this study could mistakenly contain flux from some of the identified features.

In particular, in their example plot, the contours for sunspots typically only cover the umbra, not accounting for the surrounding penumbra. It is not clear whether this will have a large effect, but certainly we expect that some strong magnetic flux associated with sunspots has been attributed to the background, or other nearby features. One other note; there was a treatment of plages in this work, from additional chromospheric observations, but a separate, specific handling of faculae in the photosphere was absent. Incorporating this could have contributed to the completeness of the study. Furthermore, a decomposition of the identified background component into regimes of strong and weak field would have provided

more clarity on the exact morphology of the SMMF, and would have likely provided evidence to conclude whether flux from AR features were, in fact, incorporated into the background.

Despite these findings, it is known that the strength of the SMMF is weaker during solar minimum, when there are fewer ARs, and stronger during solar maximum, when there are more ARs. This is suggestive that the evolution of ARs has relevance for the evolution of the SMMF.

There is a contrasting view in the literature which suggests AR flux dominates the SMMF. Kutsenko et al. (2017) claim that a large component of the SMMF may be explained by strong and intermediate flux regions. There regions are associated with ARs; using a thresholding technique they showed between 65% to 95% of the SMMF could be attributed to strong and intermediate flux, while the fraction of the occupied area varied between 2% to 6% of the disc area, depending on the chosen threshold for separating weak and strong flux. This finding suggests that strong, long-lived, inhomogeneous MFCs produce the strong rotation signal in the SMMF. Potential sources could be sunspots, plages, faculae, etc. and Kutsenko et al. (2017) discussed that there is an entanglement of strong flux (typically associated with ARs) and intermediate flux (typically associated with network fields and remains of decayed ARs). Disentangling the flux would have provided a more accurate analysis of the SMMF owing to a clearer picture of the main contributor to the SMMF.

The Sun's dynamo and hence magnetic field is directly coupled to the solar rotation. The Sun exhibits latitude-dependent and depth-dependent differential rotation with a sidereal, equatorial period of around 25 days (Howe, 2009). To Earth-based observers, the synodic rotation of the Sun is observed at around 27 days, and the SMMF displays a dominant periodicity of around 27 days due to the solar rotation (Chaplin et al., 2003; Xie et al., 2017; Bose & Nagaraju, 2018). It was also reported by Xie et al. (2017) that the surface differential rotation was observed in the SMMF with measured rotational periods of 28.28 ± 0.67 days and 27.32 ± 0.64 days

for the rising and declining phases, respectively, of all of the solar cycles in their considered time-frame.

On the other hand, Xiang & Qu (2016) utilised ensemble Empirical Mode Decomposition (EEMD) analysis to extract rotational modes in the SMMF and found two rotation periods which are derived from different strengths of magnetic flux elements. They found that a rotation period of 26.6 days was related to a weaker magnetic flux element within the SMMF, while for stronger magnetic flux elements in the SMMF, the measured rotation period was 28.5 days.

Ultimately, to date, our understanding of the SMMF and its origin remains remains open to question.

2.2 Aims

In this work an investigation of high-cadence (sub-minute) observations of the SMMF, made by Birmingham Solar Oscillations Network (BiSON) (Chaplin et al., 1996, 2005; Hale et al., 2016), was performed. The aim of the investigation was to understand the morphology of the SMMF.

This work provides a frequency domain analysis of the SMMF data, where a model was built and fit to the power spectrum of the SMMF which allowed us to understand the characteristics of its source(s).

The Rotationally Modulated (RM) signal in the SMMF was clearly observed as several low-frequency peaks in the power spectrum. In addition, the use of the high-cadence data was especially crucial for inferences on components of the SMMF with periods of less than a day at higher frequencies in the power spectrum, with the intention to determine whether the background magnetic field exhibited a stochastically excited component, which evolved on short timescales.

2.3 Data

2.3.1 Summary of the Data Set

Chaplin et al. (2003) provided the first examination of the SMMF using data from BiSON, and the work presented in this paper is a continuation of that study.

BiSON is a six-station, ground-based, global network of telescopes continuously monitoring the Sun, which principally makes precise measurements of the LOS velocity of the photosphere due to solar p mode oscillations (Hale et al., 2016). Through the use of polarising optics and additional electronics, the BiSON spectrometers can measure both the disc-averaged LOS velocity and magnetic field in the photosphere (Chaplin et al., 2003), however, not all BiSON sites measure the SMMF.

In this study we focus on the data collected by the Sutherland node, in South Africa, which was also used by Chaplin et al. (2003). Data are sampled on a 40-second cadence, and the SMMF data collected by the Sutherland station pertains the epochs from 01/1992 – 12/2012 (i.e. covering 7643 days). Over this period, the fill (i.e. duty cycle) of solar observations is low because of the combination of: (a) the fill due to using only a single site with a 40-second cadence, (b) the duty cycle needed in a given day for a 'good measure' of the Sun. Over this period, the average duty cycle of the 40-second data is $\sim 15.6\%$. If instead we take a daily average of the BiSON SMMF, the average duty cycle is $\sim 55.2\%$. This gives a higher duty cycle but a lower Nyquist frequency. Because of the much lower Nyquist frequency, modelling the background power spectral density is more challenging; therefore we use the 40-second cadence data in this work.

As a comparison to the BiSON data, SMMF observations were also acquired by the Wilcox Solar Observatory (WSO) (http://wso.stanford.edu/) (Scherrer et al., 1977b). The WSO SMMF data are sampled daily from 16/05/1975 – present day, but for comparison with the BiSON SMMF, we only used data over the same temporal range.

The WSO also measures the LOS SMMF using a Babcock-type magnetograph, which allows the measurement of the amount and sense of circular polarisation in the wings in an absorption line (Scherrer et al., 1977a). WSO uses two absorption lines for the measurement of the magnetic field: the Fe I at 5250 Å(λ5250) is used for measurement of the field, and Fe I at 5124 Å(λ5124) is used to determine the instrument's zero offset, as this line is magnetically insensitive. Scherrer et al. (1977a) describes that a single, complete observation takes $\sim$20 minutes, consisting of four 3-minute integrations. The data provided by WSO are a daily weighted mean of the observations, where the weighting used is the statistical uncertainty and the magnitude of the zero offset measured with the λ5124 line.

2.3.2 Obtaining the SMMF from BiSON

There is no catalogued BiSON SMMF data-set, so it was necessary to compute the SMMF from the available BiSON data. To acquire the SMMF from BiSON data, the method as described by Chaplin et al. (2003) was adopted; here we discuss the key aspects.

Each BiSON site employs a Resonant Scattering Spectrometer (RSS) to measure the Doppler shift of the ^{2}S$_{1/2}$ $\rightarrow$ ^{2}P$_{1/2}$ line (D1 line) of potassium, at $\sim$ 770 nm (Brookes et al., 1978). A potassium vapour cell placed within a longitudinal magnetic field Zeeman splits the laboratory line into the two allowed D1 transitions (Lund et al., 2017). The intensity of the longer wavelength (red; I_R) and shorter wavelength (blue; I_B) components of the line may be measured by the RSS almost simultaneously, by using polarising optics to switch between the red and blue wings of the line, to form the ratio given by equation (2.1), which is used as a proxy for the Doppler shift from the LOS velocity of the photosphere (see: Brookes et al., 1976, 1978; Elsworth et al., 1995a; Chaplin et al., 2003; Lund et al., 2017):

$$\mathcal{R} = \frac{I_B - I_R}{I_B + I_R} \, . \tag{2.1}$$

Photospheric magnetic fields Zeeman split the Fraunhofer line and the Zeeman-split components have opposite senses of circular polarization (Chaplin et al., 2003). Additional polarising optics are used in the RSS to manipulate the sense of circular polarization (either + or -) that is passed through the instrument. The ratio $\mathcal{R}_+$ or $\mathcal{R}_-$ is formed, and the ratios $\mathcal{R}_\pm$ would be equal if there was no magnetic field present.

The observed ratio ($\mathcal{R}_\pm$) may be decomposed as:

$$\mathcal{R}_\pm = \mathcal{R}_{\mathrm{orb}} + \mathcal{R}_{\mathrm{spin}} + \mathcal{R}_{\mathrm{grs}} + \delta r_{\mathrm{osc}}(t) \pm \delta r_{\mathrm{B}}(t)\,. \qquad (2.2)$$

where $\mathcal{R}_{\mathrm{orb}}$ is due to the radial component of the Earth's orbital velocity around the Sun, $\mathcal{R}_{\mathrm{spin}}$ is due to the component towards the Sun of the Earth's diurnal rotation about its spin axis as a function of latitude and time, $\mathcal{R}_{\mathrm{grs}}$ is from the gravitational red-shift of the solar line due to the Sun's mass (Elsworth et al., 1995b; Dumbill, 1999), $\delta r_{\mathrm{osc}}(t)$ is due to the LOS velocity of p mode oscillations, and $\delta r_B(t)$ is due to the magnetic field ($\pm$ denotes the polarity of the Zeeman-split line that is being observed) (Dumbill, 1999).

The effect of the magnetic field on the ratio is shown in Fig. 2.1, and it is clear to see from equation (2.3) that the difference between the opposite magnetic field ratios is twice the magnetic ratio residual, i.e.:

$$\mathcal{R}_+ - \mathcal{R}_- = 2\,\delta r_{\mathrm{B}}(t)\,. \qquad (2.3)$$

The BiSON RSS is measuring the velocity variation on the solar disc, and therefore a calibration from the ratio to a velocity is necessary. One method of velocity calibration is achieved by first fitting the daily observed ratio, averaged over both magnetic polarities, to a 2nd- or 3rd-order polynomial as a function of velocity, as discussed by Elsworth et al. (1995b). Here we chose to fit the ratio in terms of velocity, $\mathcal{R}_{\mathrm{calc}}(u)$, i.e.:
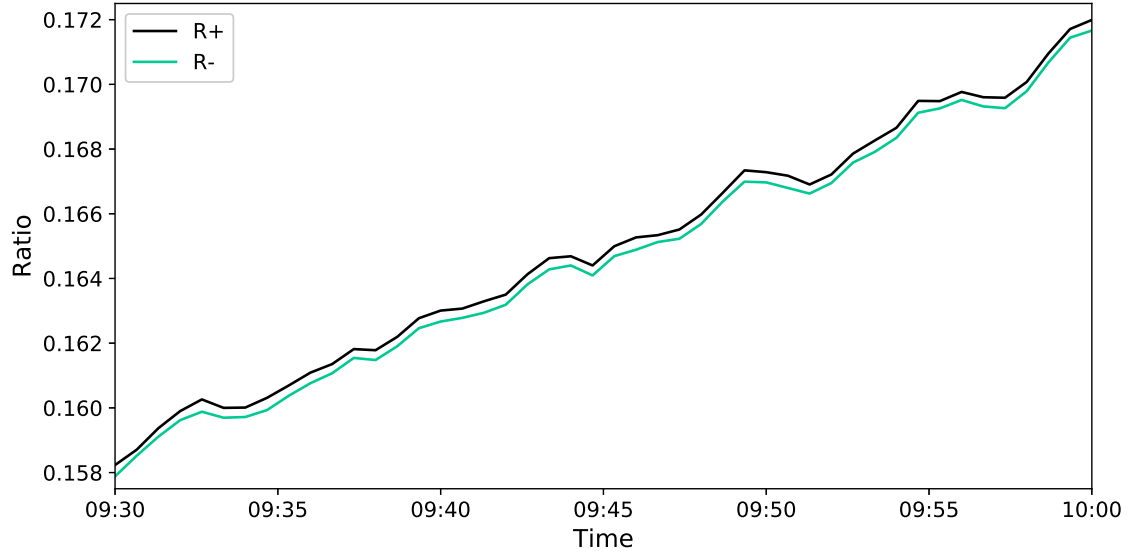
Figure 2.1: An example of the BiSON ratios data over a 30-minute period. The separation between the two ratios is due to the solar mean magnetic field. Other excursions in the individual ratios are due to the other effects measured by the RSS.

$$\mathcal{R}_{\text{calc}}(u) = \sum_n \mathcal{R}_n u^n \, , \tag{2.4}$$

where:

$$u = v_{\text{orb}} + v_{\text{spin}} \, , \tag{2.5}$$

and v_{orb} is the velocity component related to the ratio, $\mathcal{R}_{\text{orb}}$; v_{spin} is related to the ratio, $\mathcal{R}_{\text{spin}}$; and n is the polynomial order.

It is possible to see that through the removal of $\mathcal{R}_{\text{calc}}(u)$ from the observed ratios, one is left with the ratio residuals of the p mode oscillations and the magnetic field, i.e.:

$$\mathcal{R}_{\pm} - \mathcal{R}_{\text{calc}}(u) = \delta r_{\text{osc}}(t) \pm \delta r_{\text{B}}(t) \, . \tag{2.6}$$

Furthermore, conversion from ratio residuals into velocity residuals uses the calibration given by:

$$\delta v(t) = \left(\frac{d\mathcal{R}_{calc}}{dV} \right)^{-1} \delta r(t) \,. \tag{2.7}$$

In order to finally obtain the SMMF in units of magnetic field, one must combine equation (2.3) and equation (2.7) with the conversion factor in equation (2.9) (Dumbill, 1999), and the entire procedure can be simplified into:

$$B(t) = \frac{1}{2} \left(\frac{d\mathcal{R}_{calc}}{dV} \right)^{-1} \frac{(\mathcal{R}_+ - \mathcal{R}_-)}{K_B} \,, \tag{2.8}$$

where:

$$K_B = \frac{8}{3} \frac{\mu_B}{h} \frac{c}{\nu} \approx 2.89 \, \mathrm{ms}^{-1} \, \mathrm{G}^{-1} \,, \tag{2.9}$$

and μ_B is the Bohr magneton, h is Planck's constant, c is the speed of light, and ν is the frequency of the photons.

Through the application of this methodology, one acquires the SMMF as shown in Fig. (2.2a). The power spectrum of the full, 7643-day Sutherland data set is shown in Fig. (2.2b). The power spectrum shows a clear set of strong peaks at low frequency, which are due to the persistent rotation signal in the SMMF. The largest peak is the fundamental rotation frequency, and the following peaks are its harmonics.

2.4 Methodology

2.4.1 Identifying Features in the SMMF Power Spectrum

As we have 40-second cadence observations of the SMMF, we were able to investigate the power spectrum up to a Nyquist frequency of 12500 μHz. There are a number of features within the full power spectrum, shown in Figure 2.3.

The peaks between $0.1 - 2.0$ μHz are a manifestation of a persistent rotational signal in the SMMF. The distinct set of peaks indicates the existence of a long-lived, inhomogeneous, RM source. The SMMF signal exhibits a quasi-coherent
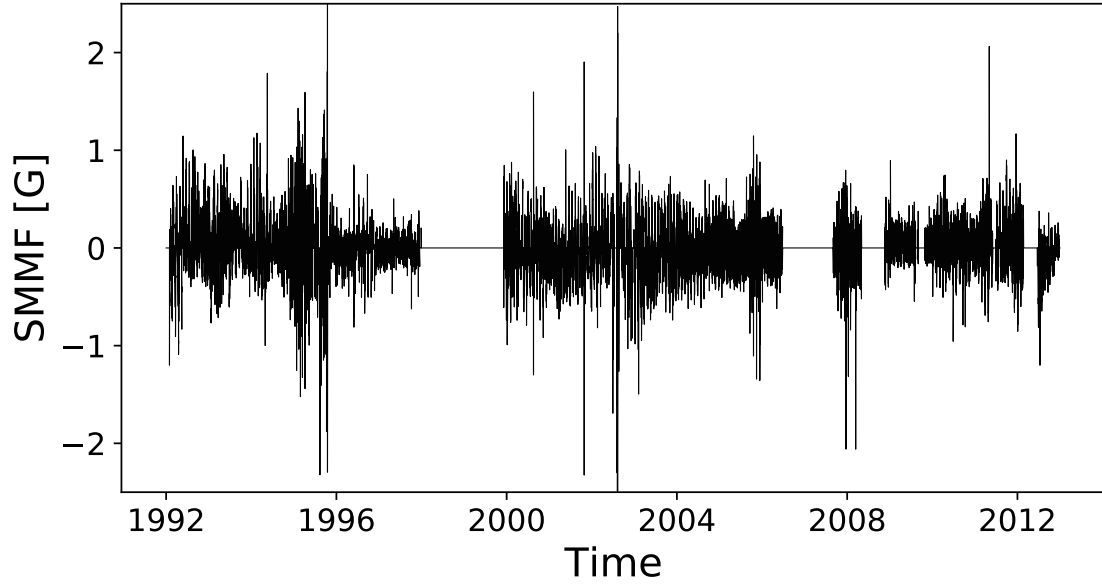
(a) BiSON SMMF 40-second cadence time series
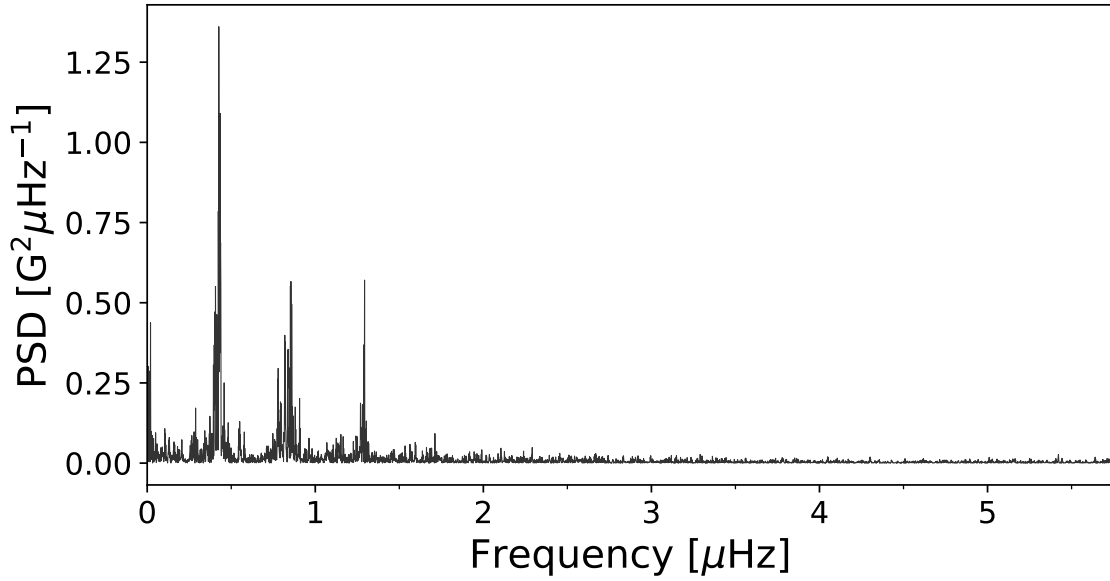
(b) Power spectral density of the BiSON SMMF

Figure 2.2: (a) 40-second cadence observations of the SMMF from the Sutherland BiSON station between 1992 and 2012. The sense of the field was chosen to match the Chaplin et al. (2003) and the WSO observations, where positive is for a field pointing outwards from the Sun. (b) Power spectrum of the SMMF on a 40-second cadence truncated to 10µHz, however, the Nyquist frequency is 12500µHz.

behaviour in the time domain, and based on the comparatively short timescales for the emergence of magnetic features compared to their slow decay (i.e. hours–days compared to weeks–months) (Zwaan, 1981; Harvey & Zwaan, 1993; Hathaway &
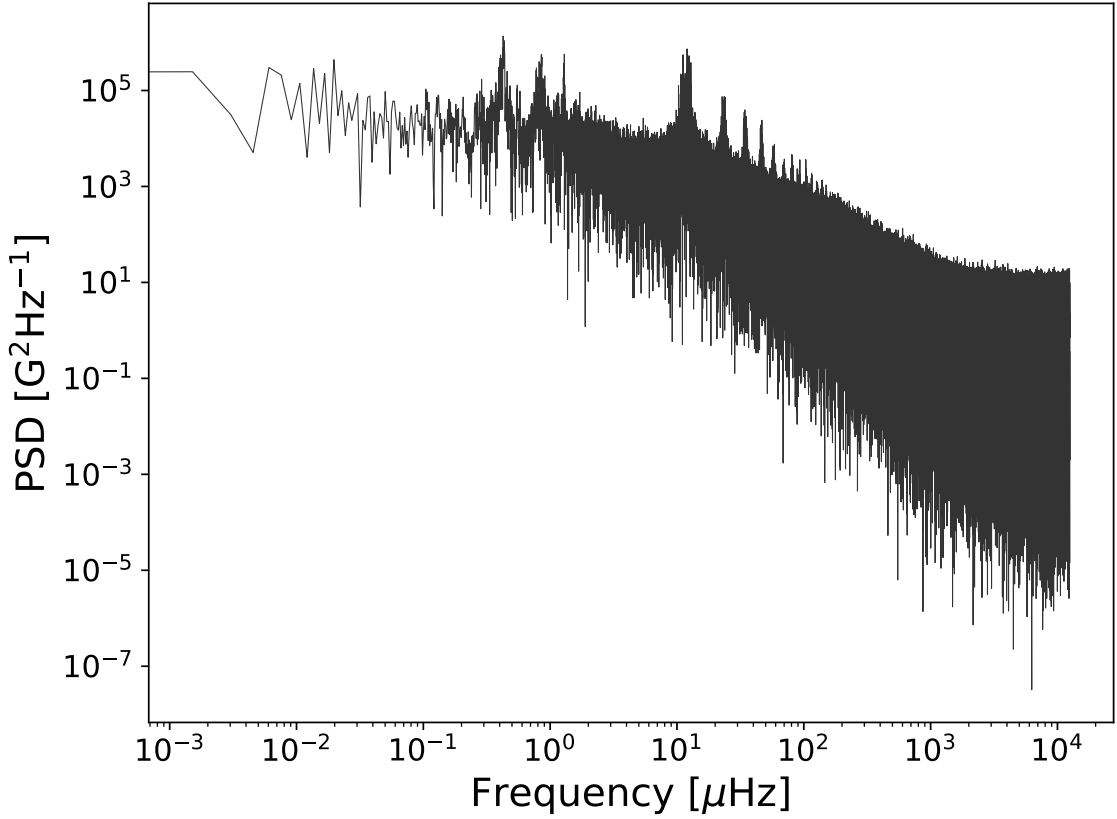
Figure 2.3: Power spectrum of 40-second cadence SMMF from the Sutherland BiSON station observed between 1992 – 2012 on a logarithmic scale up to the Nyquist frequency.

Choudhary, 2008; Dacie et al., 2016), we assume the evolution of the RM component with time is a sudden appearance and a long, exponential decay.

The high Nyquist frequency was critical in uncovering a red-noise-like component in the power spectrum. This component could arise from continuously evolving, short-lived regions of magnetic field linked to magneto-convection, akin to a random walk, which we will dub the Stochastic Background (SB) component. Analogous to the SB, is the granulation signal observed in the Doppler-velocity measurements of the solar surface (Basu & Chaplin, 2017). It is indeed possible that this is not a real feature in the data and it could also be present due to the high-cadence and low-fill of the observations.

In addition, at low-frequency there is power associated with instrumental noise and solar activity, and at very-high frequency shot-noise is captured which sets the

lower limit in power in the spectrum.

There are also side-band features in the power spectrum at multiples of 1/day $\sim$ 11.57 µHz. The side-bands are a well-known phenomena in ground-based astronomical observations. They arise from gaps in the data which are a consequence of making single-site, ground-based observations of the Sun.

The duty cycle of the 40–second BiSON observations is very low, at around $\sim$ 15%, therefore it was important to take into consideration the effect that gaps in the data have on the power spectrum. Gaps in the data cause an aliasing of power from actual signal frequencies spread to other frequencies in the spectrum, and the nature of the aliasing depends on the properties of the window function of the observations. It is also possible that the SB component is an effect of power aliasing due to the low duty cycle of the data. Hence, before modelling the power spectrum, the window function was well-characterised.

Through understanding how the duty cycle of the observations affected the power spectrum informed the way we finally parametrised the full model of the power spectrum.

2.4.2 Parametrisation of the SMMF Power Spectrum

In the frequency domain, each of the RM peaks models well as a Lorentzian distribution, similar to peak-bagging modes of solar oscillations (Handberg & Campante, 2011; Davies et al., 2014), which is due to the quasi-coherent nature of the source. The exponential decay of the RM SMMF source gives width to the peaks in the power spectrum, which we can measure to infer their lifetime.

A single, symmetric Lorentzian peak can be modelled by:

$$L_n(\nu; \Gamma, A_n, \nu_n) = \frac{2A_n^{\,2}}{\pi\Gamma} \left(1 + \left(\frac{\nu - \nu_n}{\Gamma/2} \right)^2 \right)^{-1}, \tag{2.10}$$

where ν is frequency, A_n is the Root Mean Square (RMS) amplitude of the RM component in the time-domain, Γ is the linewidth of the RM peak, ν_n is the frequency

of the RM peak, and n simply flags each peak. The mean-squared power in the time domain from the RM component of the SMMF is given by the sum of the $A_n{}^2$ of the individual harmonics in the power spectrum.

Upon closer inspection of the power spectrum it is possible to see that the peaks appear to exhibit an asymmetric shape (see Fig. 2.2 and Fig. 2.3). Taking inspiration from Howe et al. (2020), it is possible to allow for asymmetry, which is controlled by the asymmetry parameter, α, in equation (2.11) (Stancik & Brauns, 2008):

$$L_n(\nu; \Gamma, A_n, \nu_n) = \frac{2A_n{}^2}{\pi\Gamma(\nu)} \left(1 + (2X(\nu))^2\right)^{-1}, \tag{2.11}$$

where:

$$X(\nu) = (\nu - \nu_n)/\Gamma(\nu); \tag{2.12}$$

$$\Gamma(\nu) = 2\Gamma/[1 + \exp^{-\alpha(\nu - \nu_n)}]. \tag{2.13}$$

In the limit where $\alpha \to 0$, we see that $\Gamma(\nu) \to \Gamma$, thus the asymmetric expression equates to the symmetric expression.

The model function used to describe the RM signal in the power spectrum is given by equation (2.14); the sum of N Lorentzian-peaks:

$$P(\nu) = \sum_{n=1}^{N} L_n(\nu; \Gamma, A_n, \nu_n). \tag{2.14}$$

The subscript, n, describes a single peak in the power spectrum; in implementing the model we constrain the central frequency for each of the peaks such that they must be integer values of ν_0: $\nu_n = n\nu_0$. This means that we define a single rotation frequency only, and subsequent peaks are harmonics. It is worth noting explicitly that this function assumes the linewidth of each Lorentzian peak is the same; only their amplitudes and central frequencies differ.

When modelling the power spectrum we attempted the fit with both of the symmetric and asymmetric Lorentzian expressions, independently. Firstly we modelled

using the symmetric Lorentzian, and subsequently, using the asymmetric Lorentzian. This would determine whether there is a necessity for the addition of the asymmetry parameter.

Through both formulations we can measure the e-folding lifetime of the amplitude of the RM component (T_e), as it is related to the linewidth of the peak by equation (2.15):

$$\Gamma = (\pi \, T_e)^{-1} \, . \tag{2.15}$$

The low-frequency power due to instrumental drifts and solar activity can be reasonably well captured by the inclusion of a zero-frequency centred Lorentzian, i.e. Harvey-function, given by:

$$H(\nu; \sigma, \tau) = \frac{4\sigma^2\tau}{1 + (2\pi\nu\tau)^2} \, , \tag{2.16}$$

where σ is the characteristic amplitude of the low frequency signal, and τ describes the characteristic timescale of the excursions around zero in the time-domain.

Finally, the high frequency power is accounted for by the inclusion of a constant offset due to shot-noise, c.

2.4.3 Modelling the SMMF Power Spectrum

Parameter estimation was performed in a Bayesian manner using a Markov Chain Monte Carlo (MCMC) fitting routine. Following from Bayes theorem we can state that the posterior probability distribution, $p(\mathbf{a}|D, I)$, is proportional to the likelihood function, $L(D|\mathbf{a}, I)$, multiplied by a prior probability distribution, $p(\mathbf{a}|I)$:

$$p(\mathbf{a}|D, I) \propto L(D|\mathbf{a}, I) \, p(\mathbf{a}|I) \, , \tag{2.17}$$

where D are the data, and I is any prior information.

To perform the MCMC integration over the parameter space we must define a

likelihood function; however, in practice, it is more convenient to work with logarithmic probabilities. The noise in the power spectrum is distributed as χ^2 2 degrees-of-freedom (Handberg & Campante, 2011; Davies et al., 2014), therefore the log likelihood function is:

$$\ln(L) = -\sum_i \left\{ \ln(M_i(\mathbf{a})) + \frac{O_i}{M_i(\mathbf{a})} \right\} , \qquad (2.18)$$

for a model, M_i, with parameters, $\mathbf{a}$, and observed power, O_i, where i describes the frequency bin. This likelihood function assumes that all the frequency bins are statistically independent but the effect of the window function means that they are not. We handled this issue by using simulations based on the artificial data discussed in Section 2.5.1.

The prior information on each of the parameters used during the MCMC is discussed below, in Section 2.5.2.

The affine-invariant MCMC sampler `emcee` (Foreman-Mackey et al., 2013) was employed to explore the posterior parameter space. The chains are not independent when using `emcee`, therefore convergence was interrogated using the integrated autocorrelation time. We computed the autocorrelation time and found $\tau \sim 120$ steps. Foreman-Mackey et al. (2013) suggests that chains of length $\geq 50\tau$ are often sufficient. After a burn in of 6000 steps, we used 7000 iterations on 50 chains to explore the posterior parameter space, which was sufficient to ensure we had convergence on the posterior probability distribution.

2.4.4 Comparison with the WSO SMMF

To provide comparative results on the inferences from the BiSON SMMF, we repeated the analysis on the power spectrum of the WSO SMMF. The WSO data are only provided on a daily cadence, hence the Nyquist frequency is lower than for 40-second BiSON data, at $\sim 5.79\,\mu\mathrm{Hz}$, and it was not possible to observe the SB component. The analysis was therefore also repeated using the daily-averaged

BiSON SMMF, to provide a more direct comparison between BiSON and WSO.

The same parametrisation as outlined above was relevant to the modelling of the features in the WSO Power Spectral Density (PSD), and the RM peaks were fitted using a model with symmetric Lorentzian peaks and separately with asymmetric Lorentzian peaks.

2.5 Results

2.5.1 Investigation of the Window Function

Due to the low fill of data, we see the effects of daily and random gaps on the power spectrum. Periodic gaps in the data give rise to sidebands in the power spectrum and random gaps cause a more broadband shifting of power, meaning that some power from the low-frequency RM component in the power spectrum is aliased to higher frequencies. First we will concentrate specifically on the effect of daily, periodic gaps in the data. The daily, periodic gaps in the BiSON data, due to single-site observations, produce sidebands around a frequency of 1/day $\sim 11.57\,\mu\text{Hz}$ and its harmonics.

The frequency (and harmonics) of the RM component are located near zero ($\nu_0 \sim 0.4\,\mu\text{Hz}$). We are usually only interested in the real, positive frequencies but due to their close proximity to zero, they are reflected back as a product of the aliasing and hence there are negative and positive side-bands in the (positive frequency) power spectrum. When considering the aliased power, both the positive and negative side-bands must be taken into account. The aliased power is located at frequencies:

$$\nu_{n,i} = i\left(\frac{1}{\text{day}} \pm \nu_n\right). \tag{2.19}$$

where i denotes the side-band number, and n denotes the harmonic of the mode. The side-band structure implied by equation (2.19) is shown clearly in the SMMF

41

power spectrum in Figure 2.4. It is clear that we could therefore have used the predicted locations of the aliased power and incorporated them into the model for the full power spectrum. This would, however, have required us to explicitly model some $\sim$ 1100 groups of side-bands in order to cover this effect over the entire frequency range, and each group would have required a unique parameter to control the fraction of power that was contributed to the full PSD. It would have become computationally expensive to model each aliased peak and there would certainly have been room for degeneracy issues to occur.
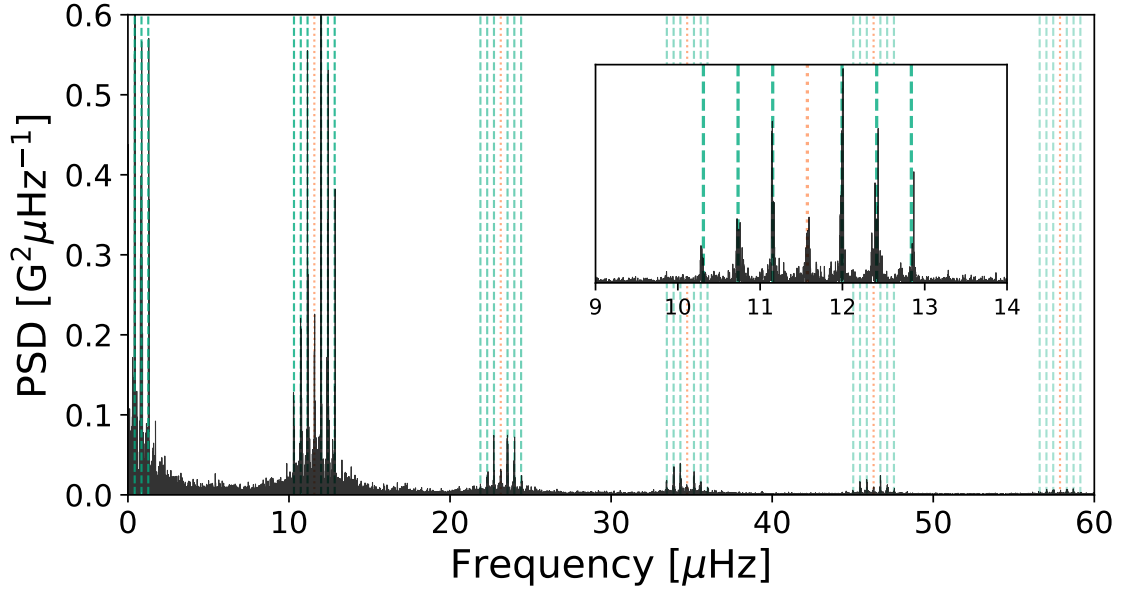
Figure 2.4: Locations of aliased power in side-band peaks. The orange, dotted-lines show the locations of frequencies at multiples of 1/day. The green, dashed-lines show the locations of the side-band peaks – harmonic frequencies reflected around multiples of 1/day. The inset shows a zoom of one set of side-band peaks around 1/day.

A more desirable, and we shall see more accurate, approach was to utilise the power spectrum of the window function itself. This approach not only takes into account the effect of daily, periodic gaps in the data, but also the more complex features that manifest in the power spectrum due to the random gaps in the data. To do this, the Fourier transform of the window function describing the duty cycle of observations was computed (i.e. $|\mathcal{F}[g(t)]|^2$), where the duty cycle function, $g(t)$, is given by equation (2.20):

$$g(t) = \begin{cases} 1 & \text{for } |B(t)| > 0 \\ 0 & \text{for } |B(t)| = 0 \end{cases}. \tag{2.20}$$

In Figure 2.5 the power spectrum of the window function is shown. Furthermore, to demonstrate the effect of the window function on the power spectrum, an artificial spectrum was simulated with a single Lorentzian peak, following equation (2.14). By computing the inverse Fourier transform, an artificial time-series was generated over the same epoch as the BiSON SMMF observations. We were then able to examine the effects of injecting gaps into the data that were concurrent with the BiSON SMMF gaps.

As well as the power spectrum of the window function, Figure 2.5 also shows the underlying noise-free peak that describes the fake data and the power spectra of the artificial data with and without the injected gaps. The power spectrum of the BiSON SMMF data is also plotted for comparison.

It is strikingly clear from Figure 2.5 that the shape of the spectrum of the window function has a remarkable resemblance to the BiSON SMMF spectrum and the output of the artificial spectrum with gaps injected. This demonstrates that the periodic window function, with such a low duty cycle, has a significant effect on the power spectrum of the input signal which not only produces the diurnal sidebands, but also a broadband spread of the power.

Due to the broadband shape of the window function power spectrum compared to the BiSON SMMF, it appears that there is actually no detectable red-noise-like, SB component in the SMMF; it is instead a manifestation of the periodic gaps in the data.

To analytically understand this effect, we can express the time series of observed data $(y(t))$ as a multiplication of the uninterrupted, underlying signal $(f(t))$ with the window function $(g(t))$, i.e.:
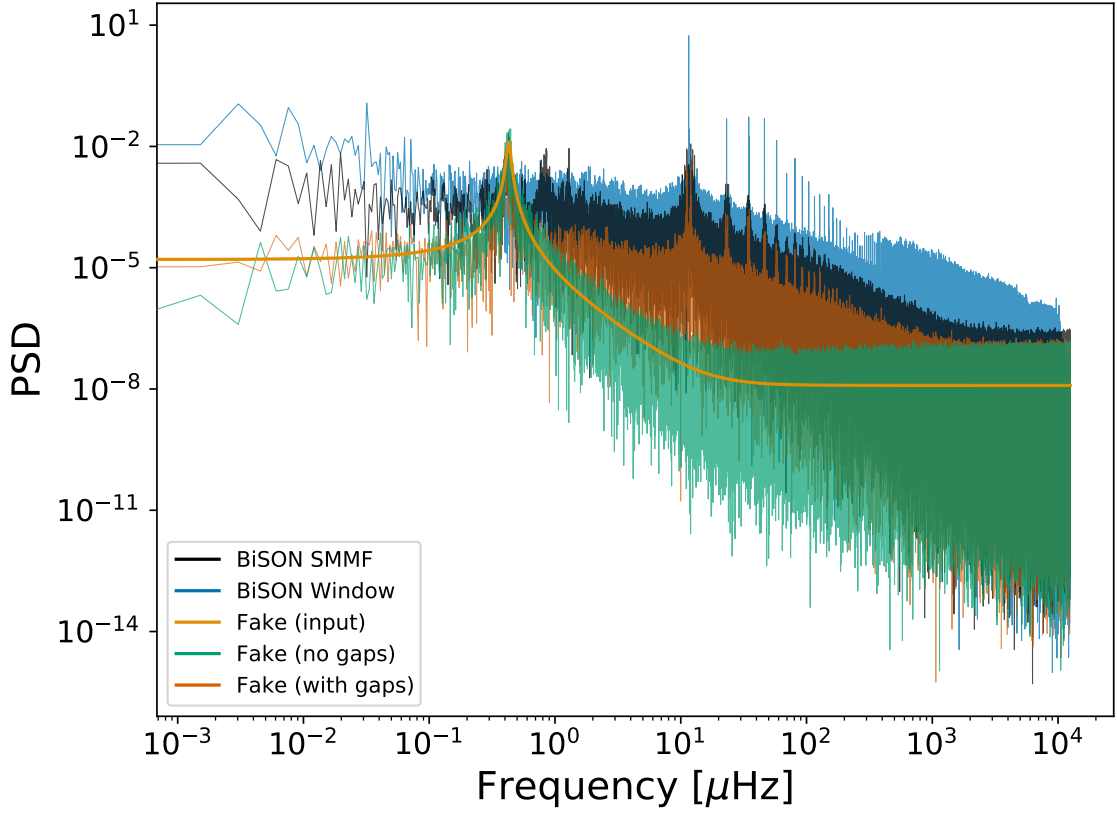
Figure 2.5: The effects of the window function on the power spectrum is shown by using a fake data set and this is compared to the BiSON power spectrum. Black line: BiSON SMMF PSD; blue line: power spectrum of the window function; green and dark-orange lines: the power spectrum of the artificial data without and with gaps, respectively; light orange line: the input peak used to generate the artificial data over-plotted. The power spectra of the BiSON SMMF and the window function have been shifted upwards by a factor of 6 and 30, respectively, for clarity.

$$y(t) = f(t)\, g(t)\,. \tag{2.21}$$

In the frequency domain, the Fourier transform of a product becomes the convolution of the transformed components. It is possible to express the observed power spectrum of data with periodic gaps in terms of the window function and the gap-free power spectrum, given in equation (2.22):

$$P'(\nu; \mathbf{a}) \;=\; P(\nu; \mathbf{a}) * |\mathcal{F}\left[g(t)\right]|^2\,. \tag{2.22}$$

Therefore to model the observed power spectrum in a robust manner, which takes

44

into account the intricacies caused by gaps in the data, we used a model which was formed of a model power spectrum, $P(\nu; \mathbf{a})$, convolved with the Fourier transform of the window function describing the duty cycle of observations ($|\mathcal{F}[g(t)]|^2$), i.e. a model described by equation (2.22), where:

$$P(\nu; \mathbf{a}) = \sum_{n=1}^{N} L_n(\nu; \Gamma, A_n, \nu_n) + H(\nu; \sigma, \tau) + c. \tag{2.23}$$

Care was taken to ensure Parseval's theorem was obeyed, and no power was lost or gained from the convolution operation:

$$\sum_{\nu} P'(\nu) = \sum_{\nu} P(\nu) = \frac{1}{N} \sum_{t} B(t)^2, \tag{2.24}$$

where N here is the number of observed cadences.

To demonstrate this method, as a proof-of-concept, we fit a model of a single Lorentzian peak, plus a shot-noise background, to the gap-free fake PSD (without the convolution) and the fake PSD using the gaps (requiring the convolution). The modelling was performed using the affine-invariant MCMC sampler `emcee` (Foreman-Mackey et al., 2013) to explore the posterior parameter space, and the results of this fit are summarised in Table 2.1.

Table 2.1: Model parameter values for the generation of artificial data, and the median posterior values for the fit to the power spectra generated with and without the gaps in the data. Numbers in brackets denote uncertainties on the last 2 digits, and all uncertainties correspond to the 68% credible intervals either side of the median.

Parameter	Input	Fit (no gaps)	Fit (gaps)	Unit
ν_0	0.42867	$0.4277\left({}^{+18}_{-18}\right)$	$0.4261\left({}^{+03}_{-03}\right)$	µHz
Γ	0.030	$0.0279\left({}^{+37}_{-36}\right)$	$0.0340\left({}^{+06}_{-06}\right)$	µHz
A	100.0	$101.2^{+7.3}_{-6.0}$	111.7 ± 0.1	mG
c	0.20	$0.1872\left({}^{+03}_{-03}\right)$	$0.1876\left({}^{+01}_{-01}\right)$	$\mathrm{G}^2\mathrm{Hz}^{-1}$

As we can see from the results in Table 2.1, the median values of the parameter posterior distributions without the gaps are in accordance with the input values, which were used when generating the artificial data, within uncertainties. When

the gaps were introduced, the median values of the parameter posterior distributions were close, but the widths of the distributions (which give implied confidence intervals) did not overlap.

Through this demonstration we observed that, as a result of the convolution in the model, the widths of the posterior distributions for the model parameters were systematically underestimated. This effect arises because we do not account explicitly for the impact of the window function convolution on the covariance of the data. To perform the full likelihood evaluation, with the correlated noise, requires large-data computational linear algebra (i.e. the inversion of an N-by-N diagonal-constant/Toeplitz matrix, where N is the size of data); unfortunately the process of fully accounting for the correlated noise in this scenario was too computationally expensive, due to the large data set with $\sim 10^7$ data points. Our ability to resolve the model parameters is well represented in the case where the convolution was not performed; this helped us to understand how the convolution affected our ability to measure the true posterior widths, which allowed us to account for the systematic underestimate of the credible regions of the posterior distributions. We assumed the for ν_0 and c, we have an accuracy of $\sim 0.5\%$ each; for Γ, an accuracy of $\sim 15\%$; for A, an accuracy of $\sim 10\%$. Using these uncertainty estimates, the parameter posterior distributions for the convolution model are in accordance with the input values.

When modelling the power spectrum of the observed BiSON SMMF, these factors allowed us to account for the systematic underestimate of the posterior widths from the convolution.

2.5.2 Modelling the BiSON Power Spectrum

As there were many data points in the power spectrum, each likelihood calculation was computationally expensive. In order to reduce the required computation, the BiSON power spectrum was cut at a frequency of 7000 µHz, as at very high fre-

quency, the spectrum purely represents the shot noise in the SMMF, and it was deemed as a sufficient limit to still fully converge on the shot noise parameter.

The BiSON power spectrum was modelled against equation (2.22) (which used equation (2.23) with $N = 4$ peaks), for both the symmetric and asymmetric Lorentzian models, using the affine-invariant MCMC sampler `emcee` (Foreman-Mackey et al., 2013) to explore the posterior parameter space. In the modelling we used uniform prior information, providing reasonable boundaries on each parameter, as detailed below.

$$\nu_0 \sim \mathcal{U}(0.38, 0.50) \, \text{µHz}$$

$$\Gamma \sim \mathcal{U}(0.00, 0.11) \, \text{µHz}$$

$$A_1 \sim \mathcal{U}(100, 350) \, \text{mG}$$

$$A_2 \sim \mathcal{U}(50, 200) \, \text{mG}$$

$$A_3 \sim \mathcal{U}(20, 150) \, \text{mG}$$

$$A_4 \sim \mathcal{U}(10, 100) \, \text{mG}$$

$$\sigma \sim \mathcal{U}(0.01, 500) \, \text{mG}$$

$$\tau \sim \mathcal{U}(0.10, 200) \, 10^6 \, \text{s}$$

$$c \sim \mathcal{U}(10^{-3}, 10^2) \, \text{G}^2 \, \text{Hz}^{-1}$$

$$\alpha \sim \mathcal{U}(-500, 0)$$

In Table 2.2 the median values of adjusted, marginalised posterior distributions for each of the model parameters are displayed, for both the symmetric and asymmetric models. The resultant posterior distributions were approximately normally distributed and there was no significant covariance between parameters, therefore uncertainties on the parameters correspond to the 68% credible intervals either side

of the median. We note the we have previously shown the convolution results in a systematic underestimate in the width of the posterior distributions and thus here we are presenting an estimation of the true uncertainties based on multiplying by the factors acquired from the artificial simulations in Section 2.5.1.

Table 2.2: Median values of the marginalised posterior distributions for each model parameter in the fit to the BiSON power spectrum using symmetric and asymmetric Lorentzian profiles. Numbers in brackets denote uncertainties on the last 2 digits, and all uncertainties correspond to the 68% credible intervals either side of the median in the adjusted posteriors. The last row in the table shows the Bayesian Information Criterion (BIC) value for each model.

Parameter	40-s symm.	40-s asymm.	Unit
ν_0	$0.4270\left(^{+18}_{-18}\right)$	$0.4278\left(^{+18}_{-18}\right)$	µHz
Γ	$0.0264\left(^{+35}_{-35}\right)$	$0.0316\left(^{+41}_{-41}\right)$	µHz
A_1	166.0 ± 10.7	178.9 ± 11.5	mG
A_2	115.9 ± 7.4	129.0 ± 8.3	mG
A_3	83.2 ± 5.3	93.5 ± 6.0	mG
A_4	32.6 ± 2.1	38.9 ± 2.5	mG
τ	51.8 ± 6.8	62.7 ± 8.2	days
σ	83.4 ± 5.4	79.1 ± 5.1	mG
c	$0.2103\left(^{+03}_{-03}\right)$	$0.2102\left(^{+03}_{-03}\right)$	$\mathrm{G^2\,Hz^{-1}}$
α	$-$	-119.8 ± 15.7	$-$
BIC	106	122	$-$

We calculated the Bayesian Informatin Criterion (BIC) to aid our model selection, to determine whether the asymmetry was truly necessary or a case of overfitting to the data. The BIC for both the symmetric and asymmetric models were ~ 106 and ~ 122, respectively. This highlighted that the model using the symmetric Lorentzian profiles was favoured, due to the lower BIC value.

The convolved model of the data, using symmetric Lorentzian peaks, is shown in Figure 2.6, over-plotted on top of the BiSON SMMF power spectrum.

The central frequency of this model, ν_0, implies a synodic rotation period of 27.11 ± 0.11 days, and hence a sidereal rotation period of 25.23 ± 0.11 days. The rotation period measured is in agreement with other literature values for the rotation signal in the SMMF (Chaplin et al., 2003; Xie et al., 2017), and is in accordance with that typically observed for ARs and sunspots.
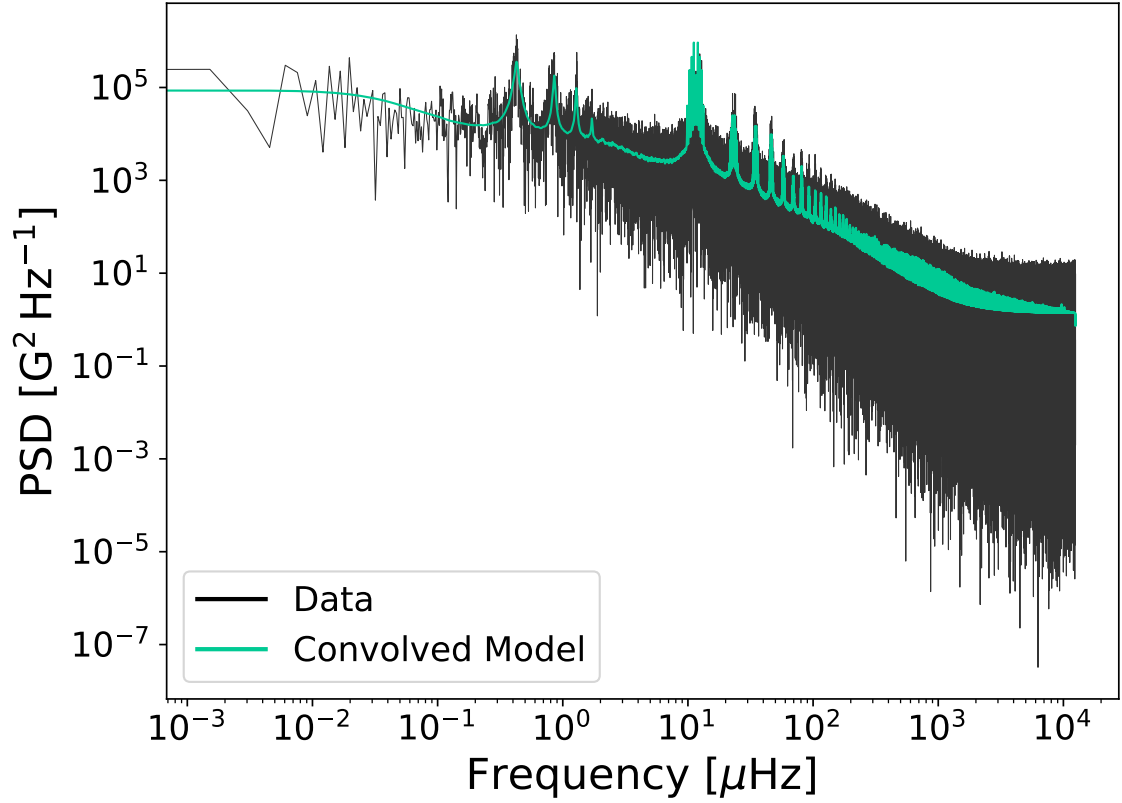
Figure 2.6: Full, modelled power spectrum of the BiSON SMMF on logarithmic axes. The data are displayed in black and the convolved model using symmetric Lorentzian peaks is shown in green.

According to the model for differential rotation given by Snodgrass (1983) and Brown et al. (1989), the measured rotation period implies the RM component of the SMMF is sensitive to a time-averaged latitude at around 12°. This latitude is consistent with those spanned by sunspots and ARs over the solar activity cycle (Maunder, 1904; McIntosh et al., 2014), and particularly during the declining phase of the solar cycle (Thomas et al., 2019). This strongly implies that the origin of the RM component of the SMMF is linked to ARs and MFCs.

Furthermore, from the measured linewidth of the Lorentzian peaks, we have calculated the lifetime of the RM component using equation (2.15). The linewidth suggests a lifetime of 139.6 ± 18.5 days, which is in the region of $\sim 20 \pm 3$ weeks. The typical lifetime of ARs and sunspots is usually on the order of weeks to months, dependent on their size (Zwaan, 1981; Schrijver & Harvey, 1994; Howard, 2001;

Hathaway & Choudhary, 2008; van Driel-Gesztelyi & Green, 2015), therefore we have measured a lifetime of the RM component which is consistent with the lifetime of ARs and sunspots. This again suggests that the source of the signal is linked to active regions of magnetic field or similar MFCs.

Taking into account the work performed by Bose & Nagaraju (2018), which showed evidence to suggest sunspots did not contribute to the SMMF, and also our concerns with their methodology, we are cautious to specify that sunspots are the source of the RM component; however, this can still not be ruled out altogether. The method of identifying ARs or strong MFCs in magnetograms by Bose & Nagaraju (2018) potentially mis-identified regions of magnetic flux associated with ARs and MFCs as background flux and it is possible that they do contribute to the SMMF. By comparison with the work carried out by Kutsenko et al. (2017), the work performed in this project agrees that the SMMF is dominated by features with properties in-line with spots, ARs, and MFCs, i.e. long-lived and making up a small fraction of the solar disc, confined to active bands of latitude.

With all this considered, we conclude that our investigation of the BiSON SMMF indicates the SMMF has its origin in the vicinity of ARs and other concentrations of strong flux that are long-lived on the solar disc and exist in active latitudes. Whether or not specifically this is due to spots or other MFCs will require further work on the magnetogram thresholding techniques investigating the SMMF.

2.5.3 Comparison to the WSO Power Spectrum

Here we present the results from modelling the WSO power spectrum; we also show the results of modelling the power spectrum of the daily-averaged BiSON spectrum, to provide a direct comparison between both observations on the same cadence.

The fill of the WSO observations over the same epoch as BiSON observations was $\sim 78\%$, and at $\sim 55\%$ for the daily-averaged BiSON observations. As the fill of the daily-averaged BiSON data was higher than the 40-cadence data, the effect of the

window function was less prominent. Nevertheless, the power spectra for both daily WSO and BiSON data were modelled using the convolution approach, as per the previous section. As, compared to the duty cycle of 40-cadence data, the fill is closer to 100%, we also expect the effect of the convolution to be less significant on the widths of the posterior distributions for each parameter, and thus the uncertainties to be more representative.

In addition, we also had to account for the sinc-function attenuation effect and reflections of power around the Nyquist frequency, due to the lower Nyquist frequency and its close proximity to the frequencies of the rotation peaks (Basu & Chaplin, 2017).

The daily-averaged BiSON power spectrum was modelled against equation (2.22) using equation (2.23) with $N = 4$ peaks, and similarly for the WSO power spectrum but with $N = 3$ peaks. Both fitting routines used the affine-invariant MCMC sampler `emcee` (Foreman-Mackey et al., 2013) to explore the posterior parameter space, using 10000 iterations on 50 chains. The convergence was again interrogated using the integrated autocorrelation time, to ensure a sufficient number of effective samples were used; hence ensuring that the posterior distribution was sampled.

In Table 2.3 the median values of marginalised posterior distributions for the model parameters are displayed, for both daily WSO and BiSON data. Reported uncertainties on the parameters correspond to the 68% credible intervals either side of the median. The systematic underestimate of the posterior width is much less of a concern with these results due to the higher duty cycle; the uncertainties are on the same order as the results not using a convolved model in Table 2.1. The convolved model for both the WSO and BiSON data, using symmetric Lorentzian peaks, are shown in Figure 2.7 over-plotted on top their respective SMMF power spectra.

The results of the fit to the daily-averaged BiSON data are similar to those for the 40-second data, however there are a few differences which arise due to the different

Table 2.3: Median values of the marginalised posterior distributions for each model parameter in the fit to the daily WSO and BiSON power spectra. Numbers in brackets denote uncertainties on the last 2 digits, and all uncertainties correspond to the 68% credible intervals either side of the median. The last row in the table shows the BIC value for each model.

| Parameter	WSO		BiSON 24-hr		Unit
	Symm.	Asymm.	Symm.	Asymm.	
ν_0	$0.4272\left(^{+05}_{-05}\right)$	$0.4290\left(^{+04}_{-04}\right)$	$0.4246\left(^{+08}_{-09}\right)$	$0.4270\left(^{+08}_{-08}\right)$	µHz
Γ	$0.0210\left(^{+16}_{-15}\right)$	$0.0210\left(^{+16}_{-15}\right)$	$0.0359\left(^{+27}_{-26}\right)$	$0.0365\left(^{+30}_{-29}\right)$	µHz
A_1	$134.8^{+3.1}_{-3.2}$	137.3 ± 3.5	$118.9^{+4.2}_{-3.8}$	$125.6^{+5.0}_{-4.4}$	mG
A_2	121.6 ± 3.4	$125.9^{+3.7}_{-3.6}$	$109.2^{+3.6}_{-3.8}$	$115.4^{+4.2}_{-4.4}$	mG
A_3	$75.1^{+3.5}_{-3.4}$	$78.9^{+4.0}_{-3.9}$	$64.6^{+3.7}_{-3.5}$	$70.1^{+4.2}_{-4.0}$	mG
A_4	–	–	$28.0^{+3.4}_{-3.3}$	$30.7^{+3.7}_{-3.6}$	mG
τ	$263.9^{+121.5}_{-83.3}$	$270.8^{+128.5}_{-84.5}$	$49.8^{+18.5}_{-12.7}$	$77.5^{+32.4}_{-22.0}$	days
σ	52.3 ± 4.6	$51.3^{+4.6}_{-4.5}$	$81.5^{+5.1}_{-1.1}$	$77.1^{+5.7}_{-5.5}$	mG
c	$11.7^{+18.7}_{-8.8}$	$11.0^{+18.4}_{-8.4}$	0.210 ± 0.011	0.210 ± 0.011	$G^2\,Hz^{-1}$
α	–	$-61.7^{+13.3}_{-15.3}$	–	$-42.1^{+12.0}_{-15.1}$	–
BIC	47	55	55	63	–
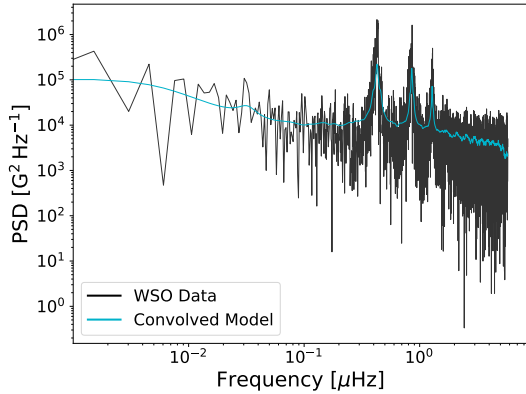
(a) WSO
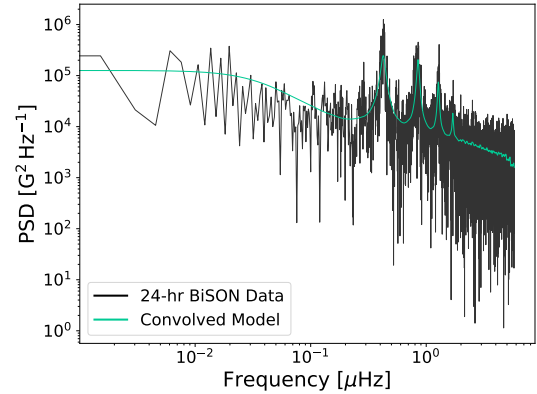
(b) 24-hr BiSON

Figure 2.7: Modelled power spectrum of (a) the WSO SMMF; (b) the daily-averaged BiSON SMMF, on logarithmic axes. The data are displayed in black and the convolved model using asymmetric Lorentzian peaks is shown in blue and green, for WSO and BiSON, respectively.

window functions and the realisations of the noise. We do however, generally, see a good agreement between the parameters. We see in Figure 2.8 that there are differences between the daily averaged and 40-second spectra; at low frequencies it is possible to see the differences in the realisations of the noise, and at higher frequencies we can see differences due to the window function aliasing. This plot

shows the possible reasons why the parameters in Table 2.3 may slightly differ from the results presented in Table 2.2.
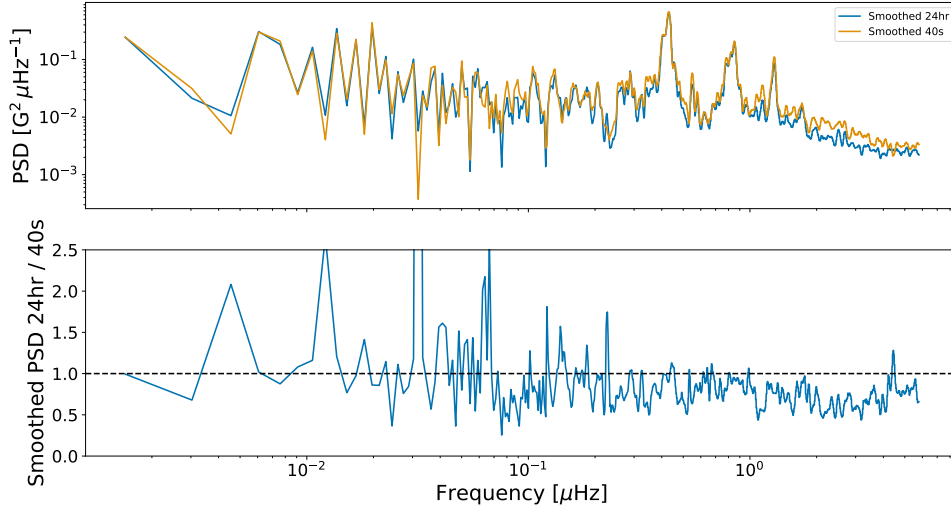
Figure 2.8: A comparison between the power spectra produced using the daily averaged BiSON data and the 40-second cadence BiSON observations. The top plot shows the log-smoothed power spectra of the daily averaged data (blue) and the 40-second data (orange). The bottom panel show the ratio of the daily averaged data power spectrum to the 40-second data power spectrum. The horizontal, dashed line indicates a ratio of 1.

The fit to the WSO power spectrum using a model with asymmetric Lorentzian profiles converged on an asymmetry parameter, but as with the 40-second analysis of the BiSON data, we calculated the BIC values for both the symmetric and asymmetric model to determine which model to select. The BIC values for the WSO models using symmetric and asymmetric Lorentzian profiles were ~ 47 and ~ 55, respectively, and the BIC values for the BiSON models using symmetric and asymmetric Lorentzian profiles were ~ 55 and ~ 63, respectively. In both cases, this highlighted that the models using the symmetric Lorentzian profiles were favoured, due to the lower BIC values.

The rotation period in the WSO data is in agreement with that measured using BiSON data to within 3σ, and this period implies a cycle-averaged latitude of around $\sim 12°$. This agrees with the conclusions drawn from our inferences of the BiSON data, that the RM source is linked to ARs.

The linewidth from the WSO data implies a RM lifetime of 175 ± 13 days,

which is in the region of ~ 25 weeks, or half a year. The WSO lifetime is in agreement with the 40-second BiSON data. However, this lifetime is inconsistent with that measured using the daily averaged BiSON data. The lifetime measured using the daily averaged BiSON data is around 50% smaller than that measured with the WSO data. A possible reason for this could be the differences arising from systematics in the fitting. When using the daily averaged BiSON data it is harder to accurately model the background because of the lower Nyquist frequency, hence we may be vulnerable to systematics impacting on the inferred widths as a higher fitted background would tend to produce narrower peak widths. These limits are still consistent however with the lifetime of large, strong ARs (Schrijver & Harvey, 1994; van Driel-Gesztelyi & Green, 2015).

As with the BiSON observations, the investigation of the WSO SMMF also indicates the origin of the SMMF is linked to ARs and MFCs that are long-lived on the solar disc and exist in active latitudes.

2.6 Discussion

2.6.1 Testing the Effects of Differential Rotation and Active Region Migration

We know the rotation period of ARs varies throughout the solar cycle as a result of solar differential rotation and latitudinal migration. As we have inferred that the RM component of the SMMF is likely linked to ARs and MFCs, we may therefore assume that the RM component is also sensitive to these effects. Here we analyse the effect of migration and differential rotation on our ability to make inferences on the lifetime of the RM component.

Several studies have modelled the the solar differential rotation, and its variation with latitude and radius of the Sun (see Beck, 2000; Howe, 2009, for an in depth review of the literature on solar differential rotation). Magnetic features have been

shown to be sensitive to rotation deeper than the photosphere; therefore, in general, magnetic features can be seen to rotate with a shorter period than the surface plasma (Howe, 2009).

Chaplin et al. (2008) analysed the effects of differential rotation on the shape of asteroseismic low-l p modes of oscillation, and showed that the consequence of differential rotation is to broaden the observed linewidth of a mode peak. The authors provide a model of the resultant profile of a p mode whose frequency is shifted in time to be a time-average of several instantaneous Lorentzian profiles with central frequency $\nu(t)$, given by equation (2.25):

$$\langle P(\nu) \rangle = \frac{1}{T} \int_0^T H \left(1 + \left(\frac{\nu - \nu(t)}{\Gamma/2} \right)^2 \right)^{-1} dt \,. \qquad (2.25)$$

The angled brackets indicate an average over time. H and Γ are the mode height (maximum power spectral density) and linewidth, respectively. The full period of observation is given by T.

Chaplin et al. (2008) also show that by assuming a simple, linear variation of the unperturbed frequency, ν_0, from the start to the end of the time-series by a total frequency shift $\Delta \nu$ (see equation (2.26)),

$$\nu(t) = \nu_0 + \Delta \nu \frac{t}{T} \,, \qquad (2.26)$$

the resultant profile of a p mode can analytically be modelled by equation (2.27):

$$\langle P(\nu) \rangle = \frac{H}{2\epsilon} \arctan \left(\frac{2\epsilon}{1 - \epsilon^2 + X^2} \right) \,, \qquad (2.27)$$

where ϵ and X are defined in equation 2.28 and equation 2.29:

$$\epsilon = \frac{\Delta \nu}{\Gamma} \,; \qquad (2.28)$$

$$X = \frac{\nu - [\nu_0 + (\Delta \nu/2)]}{\Gamma/2} \,. \qquad (2.29)$$

As the mode linewidths are broadened by this effect, we evaluated whether our ability to resolve the true linewidth of the RM component, and hence its lifetime, was affected. To evaluate this we computed the broadened profiles given by both equation (2.25) and equation (2.27), and fit the model for a single Lorentzian peak, to determine whether the linewidth is recovered.

In the first instance, we computed the broadened peak using equation (2.25). Over the duration of the observations, we computed the daily instantaneous profile, $P(\nu(t))$. The time-averaged profile, $\langle P(\nu) \rangle$, is a weighted average of each instantaneous profile, where the weights are given by the squared, daily-averaged SMMF, in order to allow a larger broadening contribution at times when the SMMF amplitude is large.

In the second instance, we computed the broadened peak using equation (2.27). Over the duration of the observations the daily frequency shift is computed, $\Delta\nu$. The time-averaged shift, $\Delta\nu$, is a weighted average, where again the weightings are given by the squared, daily-averaged SMMF.

To determine the shift in the rotation rate with migration, we used the model of the solar differential rotation as traced by magnetic features (Ω_m) given by equation (2.30), where $\mu = \cos\theta$ and θ is the co-latitude (Snodgrass, 1983; Brown et al., 1989):

$$\frac{\Omega_m}{2\pi} = 462 - 74\mu^2 - 53\mu^4 \, \text{nHz}\,. \tag{2.30}$$

Finally,the time-dependence on the latitude of the active regions used the best-fitting quadratic model by Li et al. (2001).

In both instances, the broadened peak was modelled as a single Lorentzian peak using equation (2.10), with a width equivalent to that which was inferred from modelling the BiSON power spectrum. We use `emcee` (Foreman-Mackey et al., 2013) to explore the posterior parameter space with priors similar to the fit to the full power spectrum.

Over the entire duration of the SMMF observations, the time-averaged profile was calculated, using equation (2.25), and this is shown in Fig. 2.9a. The broadened mode used the input parameters for the model using symmetric Lorentzians, outlined in Table 2.2, however, with the background parameter set to zero.

By eye, the broadened profile does not appear to have a significantly larger linewidth. The input linewidth was 0.0264 ± 0.0035 µHz, and the fit to the time-averaged broadened peak produced a linewidth of $0.0262^{+0.0038}_{-0.0037}$ µHz. The linewidth of the broadened peak under this method was rather unchanged from that of the true peak, and both linewidths are within uncertainties of each other.

Table 2.4: Input linewidth and the median posterior values of the Lorentzian model each simulation. Numbers in brackets denote uncertainties on the last 2 digits, and all uncertainties correspond to the 68% credible intervals either side of the median.

Input Value	Weighted Fit	Analytic Fit	Unit
0.0264 ± 0.0035	$0.0262^{+0.0038}_{-0.0037}$	$0.0263^{+0.0038}_{-0.0037}$	µHz

(a) Weighted
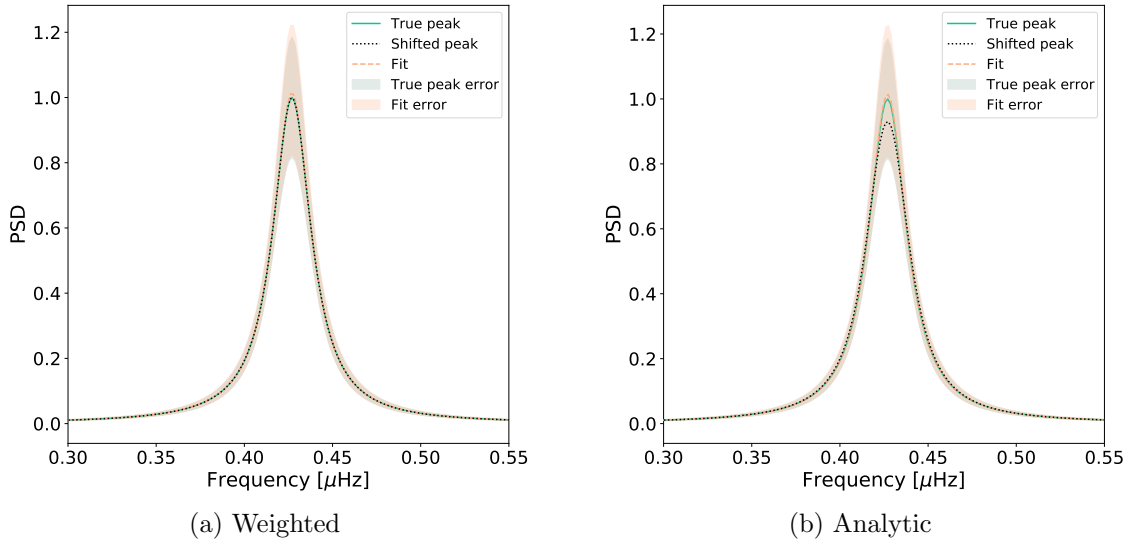
(b) Analytic

Figure 2.9: (a) Shows the Lorentzian distribution peak before and after the time-averaged broadening, and the fit to the broadened peak. (b) Shows the peak distribution before and after the analytical broadening, and the fit to the broadened peak. In both plots the broadened peaks have been shifted by the relevant frequency to overlay them on top of the true ν_0 for comparison.

The time-averaged frequency shift due to differential rotation was calculated,

much in the same way as equation (2.25), to be $\Delta\nu = 0.01285\,\mu\text{Hz}$. This shift was used to generate the broadened profile using equation (2.27). The broadened mode distribution also used the input parameters outlined in Table 2.2, however, with the background parameter set to zero.

Similar to the numerically broadened peak, by eye, the analytically broadened profile does not appear to have a significantly larger linewidth (see Fig. 2.9b). The input linewidth was $0.0264\pm0.0035\,\mu\text{Hz}$, and the linewidth of the analytically broadened peak from the fit was $0.0263^{+0.0038}_{-0.0037}\,\mu\text{Hz}$, which was within the uncertainties of the linewidth of the input peak.

These results show that both numerically and analytically, the mode broadening effect of differential rotation and latitudinal migration does not affect our ability to resolve the linewidth of the peaks. Both broadening methods applied have been shown to have a negligible effect on the measured linewidth. This result provides confidence that the linewidth in Table 2.2 is the true linewidth of the RM peaks, thus providing the correct lifetime for RM component, unaffected by migration and differential rotation.

2.6.2 Further Morphology of the SMMF using SDO/HMI Data

In Chapter **??** we acquired SDO/HMI full-disc magnetograms, using the `SunPy` python module (Barnes et al., 2020), to support our investigations into Rossby waves (see next chapter for details).

Owing to having the SDO/HMI magnetograms, which provided the capability to separately analyse the Northern and Southern Hemispheres' MMF contribution to the SMMF during the rising phase of Cycle 24 in 2011 and during solar maximum in 2014, we also investigated whether there were hemispheric differences in the data, which resulted from the opposite polarities at high latitudes and towards the poles. This served as a further analysis into other timescales which may exist

in the SMMF. In particular, we investigated whether the SMMF exhibited an anti-correlation between the two hemispheres due to the oppositely polarised field near the polar regions, as found in synoptic charts, on a time-scale of the solar cycle.

To support this investigation, we acquired the synoptic charts from SDO/HMI. It was possible to average the signal over the Northern and Southern Hemispheres of the synoptic charts, as well as the full solar surface, thus providing a comparison to the hemispheric MMF and the full disc SMMF.

To compare the magnetogram data to the synoptic charts, we smoothed the separately averaged Northern and Southern Hemispheres' MMF and the full-disc SMMF signals using a box-car filter with a window width of a Carrington period, i.e. ~ 27 days. The resultant time series was plotted along with the hemispheric mean of the synoptic charts from SDO/HMI. Figure 2.10 shows the resultant smoothed hemispheric MMF and full-disc SMMF along with the average of the synoptic charts.
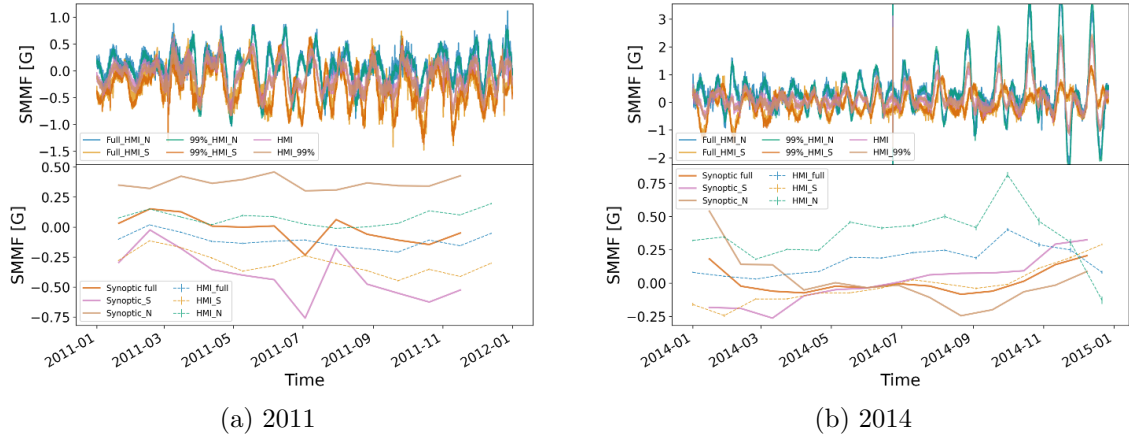

Figure 2.10: Investigations of timescales in the SDO/HMI magnetograms over 2011 and 2014. Both plots show in the top panel, the hemispheric MMF and full-disc SMMF from the magnetograms. The lower panel of each plot displays a comparison between the hemispheric and full-disc mean of the synoptic charts, compared to the box-car smoothed MMF from the magnetograms. N: Northern hemisphere; S: Southern hemisphere. Full HMI: considers the full solar disc; 99 HMI: considers only the inner 99% of the solar disc, by radius.

We can see from Figure 2.10 that there does exist a longer timescale in the hemispheric MMF when we average out the effects of the RM component. This is visible from the reversal of the field polarity in 2014. This longer timescale component re-

sembles the average of the synoptic charts, and shows the secular variation which is contributed by the solar dipole at high latitudes. This timescale is the solar activity period and can be seen particularly in Figure 2.10b. We see the beginning of a the magnetic field reversal at around solar maximum, in mid-2014, with the onset of the "rush to the poles" after solar maximum (Wilson, 1994; McIntosh et al., 2019).

Interestingly, the field reversal was located during different epochs when comparing the synoptic chart data to the visible disc, hemispheric MMF data, and was delayed in the hemispheric MMF by around 7 Carrington rotations.

Naturally, when the full-disc averaged SMMF was smoothed using the box-bar filter, the RM component was averaged out, resulting in a near-flat line. This was however expected as it was the average of the opposite hemispheres, and is consistent with the synoptic charts.

2.7   Conclusion

We have presented, for the first time, a frequency-domain analysis of over 20 years of high-cadence (40-second) BiSON observations of the SMMF.

Observations of the SMMF were computed from the Zeeman split D1 line of Potassium at ~ 770 nm, as measured by the Sutherland node of BiSON. The observations covered 7643 days over the period from $1992 - 2012$ with a cadence of 40 seconds. A frequency-domain analysis of the SMMF was performed; the short cadence and long baseline of observations gave a fine frequency resolution in the power spectrum up to a high Nyquist frequency, allowing us to probe the elements that underpin the observed SMMF.

The duty cycle for the 40-second cadence observations was very low, hence the effect of the low fill on the power spectrum of the SMMF was investigated to help inform how to best model the full power spectrum. We highlighted that although there appeared to exist a red-noise-like, stochastic background component in the power spectrum, this was a feature originating from power aliasing due to the low

duty cycle of the observations.

In the power spectrum, there was a strong peak at a frequency corresponding to the solar rotation, denoted the RM signal/component. It was also demonstrated that the low duty cycle aliased the power of the prominent peak due to the solar rotation to higher frequencies, which provided several copies of this peak at higher frequencies.

Using a model comprising of a series of Lorentzian peaks to model the RM signal, a Harvey function to account for lower frequency drifts, and shot-noise limit, which was convolved with the Fourier transform of the window function to account for the low duty cycle artefacts, we modelled the full power spectrum and measured the properties of the RM signal.

It was demonstrated that the convolution process affected the total power in the model, thus careful treatment was taken to ensure Parseval's theorem was obeyed. In addition, it was shown that the width of the posterior distributions for the parameters had been systematically underestimated, as a result of the convolution process, because we do not account explicitly for the impact of the window function convolution on the covariance of the data. We could not resolve this, but simulated data provided a comparison between a model with and without convolution which was used to provide a correction to account for the systematic underestimate of the credible regions of the posterior when modelling the power spectrum of the observed BiSON SMMF.

A comparative study was conducted on the WSO data over the same observational epoch and the modelled power spectrum provide results that were in agreement with those measured in the BiSON power spectrum.

To further investigate the SMMF and our ability to infer the properties of the source, we used simulations to analyse the effects of differential rotation and AR migrations on our ability to measure the linewidth.

Finally, a short investigation into the SMMF as measured by SDO/HMI was

61

conducted. Smoothing the data over the solar rotation period for both Northern and Southern hemispheres, separately, uncovered that the hemispheres display a longer variation, in accordance with the solar activity cycle, similar to that of the full-disc synoptic maps.

We leave the reader with the following points:

1. We have shown that there does not exist a short time-scale component in the SMMF, and the emergence of a red-noise-like signal in the power spectrum was due to the low duty cycle of the BiSON observations.

2. By modelling the peak of the RM signal as a symmetric Lorentzian profile, we found that the peak has a central frequency of $0.4270 \pm 0.0018\,\mu\mathrm{Hz}$. This measurement of the central frequency allowed us to infer the sidereal period of the RM signal to be 25.23 ± 0.11 days. This rotation suggests a magnetic feature, cycle-averaged latitude of $\sim 12°$, thus linking the source to active bands of latitude on the Sun.

3. The lifetime of the source of the RM component was inferred from the linewidth of the Lorentzian peaks to be 139.6 ± 18.5 days, which is in the region of $\sim 20 \pm 3$ weeks.

4. As a comparison, the power spectrum of the SMMF measured by WSO was also modelled and the linewidth and central frequency of the RM component were measured. The results were generally consistent with those from the BiSON data, and the conclusions inferred were in accordance.

5. The measured properties of the RM component of the SMMF are consistent with ARs. The literature advises that sunspots are not the origin of the SMMF, here we suggest that ARs and MFCs are the source of the dominant, rotation signal in the SMMF, that are long-lived on the solar disc and exist in active latitudes.

6. We have shown that our ability to determine the linewidth and hence lifetime of the RM modes was unaffected by AR migration and differential rotation.

7. Finally, a short investigation into the hemispheric contributions to the SMMF, using data from SDO/HMI, showed there is a longer-term variation which underpins the SMMF, in accordance with the activity cycle and polar field reversals.

At the time of writing, only two more of the BiSON nodes were actively measuring the SMMF (Las Campanas and Narrabri), and their measurements of the SMMF are not as stable as those measured by the Sutherland node. Sutherland has not been measuring the SMMF since 2013, however. Plans are in place to re-acquire these data in Sutherland and elsewhere, such that the frequency resolution can be further increased with a longer baseline, allowing for more accurate inferences on the SMMF morphology.

With more time on the project, it would also be useful to develop a technique similar to Kutsenko et al. (2017) and Bose & Nagaraju (2018), which allows the SMMF to be dissected into regions and features on the disc.

Bibliography

Aab A., et al., 2017, Science, 357, 1266

Aslam O. P. M., Badruddin 2012, Solar Physics, 279, 269

Aslam O. P. M., Badruddin 2015, Sol Phys, 290, 2333

Barnes a. W. T., et al., 2020, ApJ, 890, 68

Basu S., Chaplin W. J., 2017, Asteroseismic Data Analysis: Foundations and Techniques

Beck J. G., 2000, Solar Physics, 191, 47

Belov A., 2000, Space Science Reviews, 93, 79

Bose S., Nagaraju K., 2018, The Astrophysical Journal, 862, 35

Brookes J. R., Isaak G. R., Raay H. B. v. d., 1976, Nature, 259, 92

Brookes J. R., Isaak G. R., van der Raay H. B., 1978, Mon Not R Astron Soc, 185, 1

Broomhall A.-M., 2017, Sol Phys, 292, 67

Brown T. M., Christensen-Dalsgaard J., Dziembowski W. A., Goode P., Gough D. O., Morrow C. A., 1989, The Astrophysical Journal, 343, 526

Chaplin W. J., et al., 1996, Solar Physics, 168, 1

Chaplin W. J., Dumbill A. M., Elsworth Y., Isaak G. R., McLeod C. P., Miller B. A., New R., Pintr B., 2003, Mon Not R Astron Soc, 343, 813

Chaplin W. J., Elsworth Y., Isaak G. R., Miller B. A., New R., Pintr B., 2005, Mon Not R Astron Soc, 359, 607

Chaplin W. J., Elsworth Y., New R., Toutain T., 2008, Monthly Notices of the Royal Astronomical Society, 384, 1668

Dacie S., Dmoulin P., Driel-Gesztelyi L. v., Long D. M., Baker D., Janvier M., Yardley S. L., Prez-Surez D., 2016, A&A, 596, A69

Davies G. R., Broomhall A. M., Chaplin W. J., Elsworth Y., Hale S. J., 2014, Monthly Notices of the Royal Astronomical Society, 439, 2025

Dumbill A. M., 1999, PhD thesis, School of Physics and Space Research, University of Birmingham

Dunai T. J., 2010, in , Cosmogenic Nuclides: Principles, Concepts and Applications in the Earth Surface Sciences. Cambridge University Press, Cambridge, pp 1–24, doi:10.1017/CBO9780511804519.003

Elsworth Y., Howe R., Isaak G. R., McLeod C. P., Miller B. A., van der Raay H. B., Wheeler S. J., New R., 1995a. p. 392, http://adsabs.harvard.edu/abs/1995ASPC...76..392E

Elsworth Y., Howe R., Isaak G. R., McLeod C. P., Miller B. A., New R., Wheeler S. J., 1995b, Astronomy and Astrophysics Supplement Series, 113, 379

Fan K.-z., Velthuis J., 2018, arXiv:1808.10645 [astro-ph]

Fokkema D. B. R. A., 2012, PhD thesis, University of Twente

Forbush S. E., 1958, Journal of Geophysical Research, 63, 651

Foreman-Mackey D., Hogg D. W., Lang D., Goodman J., 2013, Publications of the Astronomical Society of the Pacific, 125, 306

Garca R. A., et al., 1999, Astronomy and Astrophysics, 346, 626

Giacalone J., 2010, in Schrijver C. J., Siscoe G. L., eds, , Heliophysics: Space Storms and Radiation: Causes and Effects. Cambridge University Press, Cambridge, pp 233–262, doi:10.1017/CBO9781139194532.010

Hale S. J., Howe R., Chaplin W. J., Davies G. R., Elsworth Y., 2016, Solar Physics, 291, 1

Handberg R., Campante T. L., 2011, Astronomy & Astrophysics, 527, A56

Harvey K. L., Zwaan C., 1993, Solar Physics, 148, 85

Hathaway D. H., Choudhary D. P., 2008, Sol Phys, 250, 269

Howard R. F., 2001, in , The Encyclopedia of Astronomy and Astrophysics. IOP Publishing Ltd, doi:10.1888/0333750888/2297, http://eaa.crcpress.com/0333750888/2297

Howe R., 2009, Living Reviews in Solar Physics, 6

Howe R., Hill F., Komm R., Chaplin W. J., Elsworth Y., Davies G. R., Schou J., Thompson M. J., 2018, ApJL, 862, L5

Howe R., et al., 2020, Mon Not R Astron Soc Lett, 493, L49

Inceoglu F., Knudsen M. F., Karoff C., Olsen J., 2014, Sol Phys, 289, 1387

Janardhan P., Fujiki K., Ingale M., Bisoi S. K., Rout D., 2018, Astronomy and Astrophysics, 618, A148

Kane R. P., 2014, Solar Physics, 289, 2727

Kotov V. A., 2008, Astron. Rep., 52, 419

Kotov V. A., 2012, Bull.Crim. Astrophys. Observ., 108, 20

Kutsenko A. S., Abramenko V. I., Yurchyshyn V. B., 2017, Sol Phys, 292, 121

Li K. J., Yun H. S., Gu X. M., 2001, AJ, 122, 2115

Lund M. N., Chaplin W. J., Hale S. J., Davies G. R., Elsworth Y. P., Howe R., 2017, Mon Not R Astron Soc, 472, 3256

Maunder E. W., 1904, Mon Not R Astron Soc, 64, 747

Mavromichalaki H., Paouris E., Karalidi T., 2007, Sol Phys, 245, 369

McIntosh S. W., et al., 2014, ApJ, 792, 12

McIntosh S. W., Leamon R. J., Egeland R., Dikpati M., Fan Y., Rempel M., 2019, Sol Phys, 294, 88

Mishra V. K., Mishra A. P., 2016, Indian J Phys, 90, 1333

NMDB 2018, NMDB Event Search Tool (NEST), http://www.nmdb.eu/nest/

Owens M. J., Forsyth R. J., 2013, Living Rev. Sol. Phys., 10, 5

Pacini A. A., Usoskin I. G., 2015, Sol Phys, 290, 943

Paouris E., Mavromichalaki H., Belov A., Eroshenko E., Gushchina R., 2015, J. Phys.: Conf. Ser., 632, 012074

Parker E. N., 1965, Planetary and Space Science, 13, 9

Pesnell W. D., Schatten K. H., 2018, Sol Phys, 293, 112

Plachinda S., Pankov N., Baklanova D., 2011, Astronomische Nachrichten, 332, 918

Ross E., Chaplin W. J., 2019, Sol Phys, 294, 8

Scherrer P. H., Wilcox J. M., Howard R., 1972, Sol Phys, 22, 418

Scherrer P. H., Wilcox J. M., Kotov V., Severnyj A. B., Severny A. B., Howard R., 1977a, Solar Physics, 52, 3

Scherrer P. H., Wilcox J. M., Svalgaard L., Duvall Jr. T. L., Dittmer P. H., Gustafson E. K., 1977b, Solar Physics, 54, 353

Schrijver C. J., Harvey K. L., 1994, Solar Physics, 150, 1

Severny A. B., 1971, Quarterly Journal of the Royal Astronomical Society, 12, 363

Singh M., Singh Y. P., Badruddin 2008, Journal of Atmospheric and Solar-Terrestrial Physics, 70, 169

Snodgrass H. B., 1983, The Astrophysical Journal, 270, 288

Stancik A. L., Brauns E. B., 2008, Vibrational Spectroscopy, 47, 66

Svalgaard L., Wilcox J. M., Scherrer P. H., Howard R., 1975, Sol Phys, 45, 83

Thomas S. R., Owens M. J., Lockwood M., 2014a, Sol Phys, 289, 407

Thomas S. R., Owens M. J., Lockwood M., Scott C. J., 2014b, Solar Physics; Dordrecht, 289, 2653

Thomas A. E. L., et al., 2019, Mon Not R Astron Soc, 485, 3857

Tomassetti N., Orcinha M., Baro F., Bertucci B., 2017, ApJL, 849, L32

Upton L. A., Hathaway D. H., 2018, Geophysical Research Letters

Usoskin I. G., Kananen H., Mursula K., Tanskanen P., Kovaltsov G. A., 1998, Journal of Geophysical Research: Space Physics, 103, 9567

Van Allen J. A., 2000, Geophysical Research Letters, 27, 2453

Wilson P. R., 1994, Solar and Stellar Activity Cycles. Cambridge Astrophysics, Cambridge University Press, Cambridge, doi:10.1017/CBO9780511564833, https://www.cambridge.org/core/books/solar-and-stellar-activity-cycles/49EFD2ED430403044DEB7B7177F77DAF

Wu C. J., Usoskin I. G., Krivova N., Kovaltsov G. A., Baroni M., Bard E., Solanki S. K., 2018, A&A, 615, A93

Xiang N. B., Qu Z. N., 2016, AJ, 151, 76

Xie J. L., Shi X. J., Xu J. C., 2017, The Astronomical Journal, 153, 171

Zwaan C., 1981, NASA Special Publication, 450

van Driel-Gesztelyi L., Green L. M., 2015, Living Rev. Sol. Phys., 12, 1